Master's Theses   Master's Theses and Graduate Research

2006

MM5 simulation of transport patterns during a Middle-East summer ozone period

Shoukri J. S Kasakseh
San Jose State University

Follow this and additional works at: https://scholarworks.sjsu.edu/etd_theses

MM5 SIMULATION OF TRANSPORT PATTERNS DURING

A MIDDLE-EAST SUMMER OZONE PERIOD

A Thesis Presented to

The Faculty of the Department of Meteorology

San Jose State University

In Partial Fulfillment

of the Requirements for the Degree

Master of Science

by
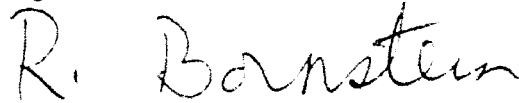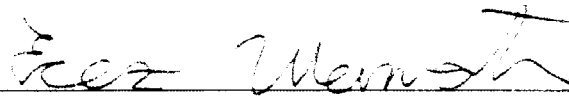
Shoukri J. S. Kasakseh

August 2006

APPROVED FOR THE DEPARTMENT OF METEOROLOGY

_____

Prof. Douglas M. Sinton, Chair

_____

Prof. Robert D. Bornstein

_____

Dr. Erez Weinroth

APPROVED FOR THE UNIVERSITY

_____

ABSTRACT

MM5 SIMULATION OF TRANSPORT PATTERNS DURING A MIDDLE-EAST

SUMMER OZONE PERIOD

by Shoukri J. S. Kasakseh

Meteorological conditions over the West Bank, Gaza, and Israel were studied

during average-summertime surface-O_3 conditions. MM5 was run with three nested

domains (min grid spacing of 1.67 km). Minimum biases resulted when MM5 input deep

soil temperature was lowered by $9^{\circ}C$ and its soil moisture content was capped at 10%.

MM5 surface flow patterns correctly reproduced the observed diurnal variation of coastal

and slope flows.

The 700 hPa flow was dominated by the Azores High and a low-pressure center

north of the area, while surface interactions involved the High and the Persian Low. As

the Low was only north of the study area, surface O_3 did not approach episode levels. The

observed O_3 peak occurred at 1100 LST near the coast. While this peak is several hours

earlier than at most other sites, simulations have shown a larger (and later) peak over

Jordan due to emissions from a large coastal power plant.

.

Acknowledgements

Table of Contents

List of Tables

List of Figures

x

1. Middle-East Introduction

a. Air-Pollution Meteorology

Most of coastal Israel and the West Bank have a Koeppen dry-summer subtropical climate (Csa), while its southern part (including the Gaza Strip) has a semi-arid climate (Bsa). Middle East General Circulation (GC, see Appendix A for list of acronyms) and synoptic influences on these climates have been summarized by Dayan and Rodnizk (1999), e.g., the dominant wintertime large-scale Siberian-high pressure system has the Middle East on its southwestern edge.

In summer, land areas warm, the Siberian-high disappears, and the Persian Trough thermal low forms to the east (over the Persian Gulf) as part of the Indian Monsoon low. To the west, the Azores high and its subsidence result in a shallow elevated-inversion layer that inhibits vertical motions and mixing. It also produces clear skies, warm surface temperatures, strong nocturnal surface-based inversions, and arid cloud-free climatic conditions, except during early morning hours when coastal stratocumulus or stratus clouds form.

Mesoscale coastal land/sea circulations, in combination with mountain/valley slope-flows, modify the above large-scale flow patterns. Nocturnal near-surface offshore land breezes form due to surface cooling during periods with weak opposing large-scale horizontal pressure gradients. Such flows are strongest during winter, can be dominated by down slope (katabatic) mountain breezes (Doron and Neumann 1977), and are strongest with reinforcing nocturnal low-level jets (LLJs) (Blackadar 1957; Mahrt 1981; McNider et al. 1988).

1

Daytime summertime onshore near-surface sea-breeze flow forms due to land-surface heating. Such flows, first investigated in 1799 on Lake Erie (Ellicott 1799), were found to be caused by land-sea temperature (and thus pressure) gradients, but are reinforcing by anabatic (upslope) winds along inland mountain chains. The orientation and speed of ambient-winds either reinforce or inhibit the inland propagation-speed and penetration of sea breeze flows, while sea breeze fronts arise when ambient winds oppose them (Arritt 1989). Coriolis forcing results in a maximum inland sea breeze penetration at 30^0N because of resonance between the diurnal-heating and inertial-oscillation periods (Rotunno 1983; Yan and Anthes 1987). Sea and land breeze development is also influenced by coastline-curvature (Neumann 1951), i.e., convex/concave coasts cause flow-divergence/convergence that weakens/strengthens sea breeze fronts.

Early investigations of Eastern Mediterranean sea-breeze flows by Neumann and Mahrer (1971) found deep inland penetration (to about 24 km), as the area is close to the Coriolis resonance latitude (Neumann 1984; Arritt 1989). Its breezes are also enhanced by the concave coast (Neumann 1951; Alpert *et al.* 1988) and by anabatic winds from the northern (Carmel and Galil) coastal hills and the central-southern (Shomron and Judea) inland hills (Perlin and Alpert 2000).

Photochemical O_3 episodes occur around the world during summer in association with anticyclonic conditions and their associated low wind-speeds, high insolation, and shallow mixing depths (Seinfeld and Pandis 1998). Emissions of urban precursors, i.e., NO_x and VOCs undergo photochemical transformation in the presence of solar radiation to create 0_3.

2

Summer measurements at inland rural surface-sites 50 km east of the flat Tel Aviv urbanized coastal-plain show afternoon O_3 frequently exceeding the Israeli ambient half-hour standard (125 ppb), occasionally reaching 150 ppb (Matveev *et al.* 2002). Back-trajectory analyses by Hebestreit *et al.* (1999) showed that only air masses passing over the Tel Aviv area into a northwesterly background flow caused elevated O_3 levels over Jerusalem.

High NO_x/SO_2 ratios indicated that ozone-precursors originated mainly from sur-face-transportation fossil-fuel combustion. Ozone levels increased with increasing inland distance, as sufficient time (3-5 h) is required for air masses to reach inland rural sites and to allow photochemical processes to generate significant ozone (Seinfeld and Pandis 1998). These NO_x-sensitive photochemical processes thus mainly occur over rural areas in aged air-masses.

Hebrew Univeristy Jerusalem Israel (HUJI) summertime airborne measurements by Peleg *et al.* (1994) at 300 m AGL from 1994 to 1997 detected afternoon O_3 exceeden-ces over the Shomron and Judain Hills during 19 of 32 flights; this study is herein refered to as HUJI97. A well mixed convective boundary layer implies that these concentrations were similar to surface values.

Dayan and Koch (1996) and Dayan and Levy (2002) have identified the following three synoptic patterns that account for 74% of O_3-episodes over the study area: winter-time high pressure east of the Mediterranean (25%), springtime "Yam-Suf" (Red Sea) trough with a north to south axis over Israel (29%), and summertime shallow Persian Gulf thermal trough over Israel (20%). The latter produce high O_3 because they are

3

caped by the Northern African sub-tropical High, which produces: subsidence warming, stabilization, shallow mixed-layers, sunshine, and rapid photochemistry (Dayan *et al.* 1988; Hashmonay *et al.* 1991).

b. *Meso-modeling studies*

Three-dimensional numerical Eulerian meso-met model output (i.e., wind velocity, temperature, and diffusivity) have been used as input to photochemical models to simulate atmospheric transport, diffusion, and photochemical processes for regulatory studies in a variety of cities. An important prerequisite component of such an effort is an emissions inventory of the primary pollutants that undergo transformation (Giovannoni *et al.* 1995; Sillman *et al.* 1997; Svensson 1998; Ziomas *et al.* 1998).

Photochemical models were used by Lu *et al.* (1997) to study O_3 in the subtropical hilly coastal urbanized Los Angeles Basin. Results showed that sea-breeze and mountain winds inject pollutants into the base of the West Coast elevated subsidence in-version, which results in a reservoir of trapped photochemically-aged pollutants that fumigate downward during the following morning to increase near-surface concentrations. A similar study for Athens, also a hilly coastal urban area, by Clappier *et al.* (2000) found O_3 levels also influenced by re-circulating (including over-water transport) aged-pollutants. Similar transport-mechanisms also occur in the Middle-East, given its similar coastal topography and climate (Dayan and Kock 1996).

The 3-D RAMS meso-met (Pielke *et al.* 1992) and Lagrangian particle (Walko *et al.* 1995) models were used by Dean *at al.* (2002) to study trans-boundary pollution transport-patterns from major coastal sources in the Tel Aviv and Gaza Strip areas during the

4

HUJI97 study-period. Results showed influences from daytime combined sea-breeze and upslope flows in transporting material inland and upwards over the coastal mountains. Simulated particle-patterns correlated well with airborne and surface O_3 patterns over inland Jerusalem.

Weinroth (2005) used RAMS 3-D met fields as input to the CAMx photochemical model; the first reference will herein be referred to as Wein05. His inner horizontal RAMS grid spacing was 1.25 km, while his first vertical grid-box top was at 125 m AGL. Results were compared to observations from 16 Israeli surface air-quality monitoring stations for two summertime HUJI97 observational periods.

Results showed that during the HUJI97 flight period (1500 LST or 1200 UTC on 1 August); coastal power-plant emissions produced an O_3-peak at 300 m of 113 ppb at a site 90 km inland (over Irbid, Jordan, where no observations were available). Observed surface concentrations over Israel (due mainly to surface-transportation emissions) on that day peaked earlier (1100 LST) at 72 ppb at Maapil (10 km inland and 72 km northwest of Jerusalem). The second-highest value (67 ppb) at this time was over Modiin, 30 km inland and the closest site to Jerusalem (25 km to its northwest). The corresponding Maapil CAMx peak was correctly located (given the sparseness of the network in that region), occurred an hour earlier than observed, and was 10% over-predicted, while the Modiin peak was correctly timed, but was 20 % over predicted. While predicted surface flow-patterns were shown, they were not compared to observed patterns. It was thus not possible to evaluate contributions to the O_3 over predictions from modeling-system components, i.e., RAMS met, emission inventory, and CAMx modules.

Whereas the Wein05 study of the HUJI97 ozone-episodes used the RAMS meso-met and CAMx photochemical numerical-models, it focused more on event chemistry and less on meteorology. The current study (kasakseh 2006) uses the MM5 meso-met model (with a finer near-surface vertical grid resolution) to thus focus on both large-scale (GC and synoptic) and meso-scale transport-patterns during the same period.

2. Methodolgy

The current study uses MM5 to simulate large-scale and mesoscale met conditions during the HUJI97 aircraft-observational period simulated by Wein05, with simulations from 29 July to 3 August and with a focus on the O_3 patterns on 1 and 2 August. The study first carries out a detailed analysis of available IMS observed met-data and weather charts to better understand large-scale 700 hPa and PBL mesoscale pollutant transport-patterns.

a. MM5 model

MM5 is the Fifth-Generation PSU/NCAR prognostic numerical mesomet model (Grell *et al.* 1994; Dudhia 1993, 2001; Dudhia and Bresch 2002; Dudhia *et al.* 2003;). It is non-hydrostatic, fully compressible, terrain following, and with vertical sigma-coordinates on a nested horizontal rectangular Arakawa-Lamb (1977) B staggered-grid. Its split leapfrog, semi-implicit time-steps allow sound waves to be treated semi-implicitly with short time steps, while its spatial differences are centered and second-order.

Preprocessors are first run to produce required MM5 inputs. TERRAIN first prepares domain boundaries, grid spacings, and map projections, and then horizontally interpolates regular latitude-longitude terrain elevations and land-use/land-cover fractions onto those domains. REGRID then first reads selected gridded pressure-level large-scale output (from ECMWF in current application) and then linearly interpolates them to the MM5 horizontal grid from TERRAIN. LITTLE_R next blends synoptic rawinsonde and surface observations with pre-processor REGRID output-fields by use of an objective-an-

alysis scheme. Observations are then compared to the interpolated "first-guess" ECMWF fields, and if differences exceed input threshold values, they are discarded.

INTERPF next converts REGRID and Little_R outputs into MM5 inputs. It inputs REGRID, LITTLE_R, or INTERPB data to generate model ICs, as well as lateral and lower BCs. Diagnostic-adjustment of base-state pressure, temperature, and height values, as well as of vertical wind speed and perturbation pressure, is next performed. After reformatting, it outputs the MM5 IC and lower BC values, as well as their lateral BC values (and tendencies) in a boundary-zone.

b. MM5 application

The Wein05 HUJI97 simulations included three domains (Fig. 1) in a polar stereographic projection, with: Domain-1 horizontal grid spacing of 20 km over the Eastern Mediterranean to capture background synoptic forcing; Domain-2 at 5 km over Israel, West Bank, and Gaza to simulate mesoscale sea/land and mountain/valley flows; and Domain-3 at 1.25 km along the Tel Aviv-Jerusalem corridor to reproduce inter-city transport patterns. Domains contained 45 x 45, 74 x 54, and 146 x 218 horizontal grid points, respectively, and had 24 vertical levels (up to 11 km), with grid cells that ranged from 125 m near the ground to 1100 m at the uppermost level.

Topography heights were obtained from USGS GTOPO 30 sec resolution data (http://edcdaac.usgs.gov/ gtopo30/gtopo30.html), with local land-use derived from Digital Terrain Model data (25 m resolution) for the second and third grids, while land use for the first grid was obtained from USGS GTOPO30. His simulations started at 0000

UTC on 1 August, ended 72 h later, and were initialized and updated every 6 h with ECMWF met-data.

The current application uses MM5 with a Lambert-conformal map projection (suitable for mid latitude regions) with three nested horizontal-domains (Fig. 2) with grid spacing of 15, 5, and 1.67 km. With the selected two-way nesting option (with continuous feedback at every time-step to each next-outer domain), a ratio of 3:1 must be used between successive grid-domain grid-size. The current outer-domain (Domain-1) is centered at 32.0°N and 35.0°E, with Domain-2 selected to overlap as closely as possible to that of Wein05. Domains 1 to 3 have 59 x 61, 55 x 76, and 58 x 85 horizontal grid-points, respectively.

USGS terrain-height (GTOPO30) data were used at the following resolutions: 5 min (~9 km), 2 min (~4 km), and 30 sec (~0.9 km) in Domains 1-3, respectively. Land-use distributions for all three grids were obtained from the 24-category USGS data set. Other MM5 options selected include: Dudhia (1993) explicit simple-ice moisture, Grell *et al.* (1994) cumulus parameterization, and Gayno-Seaman (Gayno 1994) level 1.5 PBL TKE. ECMWF output (archived at NCAR) on a 2.5^0 lat x 2.5^0 long grid at 0000 and 1200 UTC were used as the "first-guess" ICs and BCs.

c. MM5 simulations

Data from the surface mesoscale HUJI97 network (Fig. 3) includes 58 sites (Table 1) with 10 m winds (18 showed incomplete data) and 39 (of the 58) sites with 2 m temperatures. These observations will be compared to MM5 Domain-2 (i.e., it contains all stations) lowest half-sigma (~10 m) temperature, wind speed, and wind direction values

9

from the grid-cell closest to each observational site. Data from the seven sites in the southern part of Domain-2 were made available near the end of the project. As they produced statistical biases much larger than those already obtained from the more numerous northern sites, they were not included in the statistical results shown below. IMS rawinsonde-soundings (up to 2 km) were obtained every six hours at Bet Dagan from 29 July at 0000 UTC to 4 August at 0000 UTC. Near-surface O_3-observations from 16 sites (Table 2) in the northern part of the study area (Fig. 4) were also available.

Simulations began at 0300 LST (0000 UTC) on 29 July and ran for five days. The GrADS graphical system was used to display MM5 output after a 12 h spin-up period. MM5 winds were plotted in mesoscale format: full barbs and flags represent 1 and 5 m s^{-1}, respectively. The following three simulations were performed:

- Run-1: Original-Case used "off-the-shelf" inputs into MM5.
- Run-2: Cool Soil-Case used uniformly reduced (by –9 K) lower BC deep-soil temperature, set in preprocessor INTERPF.
- Run-3: Dry Cool Soil-Case used change in Run 2 and a reduced (to a max of 10%) IC soil-moisture, set in MM5 LANDUSE input table.

As Run-3 results were the most accurate, they will be discussed below.

3. Results

Large-scale ECMWF model output-fields are first compared to concurrent observed IMS surface and 700 hPa synoptic pressure-patterns, following the procedure of Boucouvala *et al.* (2003) and Bornstein (2006) for the South Coast Air-Basin. The procedure thus evaluates whether the input fields will provide accurate IC and BC (GC- and synoptic-forcing) for MM5, whose results are then reviewed.

a. Synoptic forcing

On 29 July 1997, the 700-hPa IMS pattern (Fig. 5a) at 0000 UTC (0300 LST) shows the eastern-Mediterranean dominated by a low-pressure system (central height 3090 m and southern-extent arbitrarily defined by its 3120 m contour) that splits the inland lobe of the Azores high into southwestern-boundary and northeast-segments. A west-east protrusion from the southwestern high (eastern-extent arbitrarily defined by its 3180 m contour) penetrates slightly inland of the western Saudi Arabian coast. Concurrent 700-hPa ECMWF pressures (serve as MM5 ICs and BCs) well represent the position and strength of the low, both highs, and protrusion into Saudi Arabia (Fig. 6a).

As ECMWF pressure patterns can show additional small-scale details not seen in IMS observational patterns, the southwest-northeast orientation of its protrusion is probably more accurate than the west-east IMS pattern. Concurrent ECMWF winds in a sub-domain over the core study area (Fig. 7a) show the northern part of the domain influenced by westerly winds along the southern edge of the low located north of the domain. The two anticyclonic circulations in the southern part of the domain are associated with the protrusion into Saudi Arabia.

11

By 0000 UTC on 30 July (not shown), the IMS low-center moved southward and expanded to the south. The southwestern high strengthened by 10 m, the northeastern high weakened in association with the cyclonic intrusion, as did the protrusion, which retreated south-westward from Saudi Arabia. The concurrent ECMWF pattern shows the low correctly expanded southward, which correctly further split the highs, pushed the protrusion westward from Saudi Arabia.

A day later (Fig. 5b), the IMS low was again greatly expanded southward to the core study-area, further splitting the highs and pushing the west-east protrusion further westward. The concurrent ECMWF pattern (Fig. 6b) correctly showed this expansion, but while the protrusion was also correctly pushed westward, its orientation was more north-south than before. Concurrent winds (Fig. 7b) now show most of the core study-area with a cyclonic/southwesterly flow, in association with the southward movement of the low into the area. Anticyclonic circulation still exists only in the southeastern part of the domain, in association with the weakened protrusion over Saudi Arabia.

By 0000 UTC on 1 August, the southern-edge of the low was now far south of the study area (Fig. 5c), which pushed the protrusion from the high even further westward. The concurrent ECMWF 700 h-Pa pressure pattern (Fig. 6c) captured both these changes, while its cyclonic circulation has thus increased (Fig. 7c). A day later, the IMS low started to retreat back northward (Fig. 5d), while the high protrusion remained unchanged. While the ECMWF low (Fig. 6d) also correctly retreated to its initial position north of the study-area, its more-resolved protrusion expanded eastward. Concurrent winds (Fig. 7d) thus showed a return to the westerly flow from the start of the period.

12

The IMS surface chart at 0000 UTC on 29 July (Fig. 8a) shows the eastern edge of the Azores high northwest of the study area, with an eastward projection from its southern lobe (arbitrarily marked by its 1008 hPa contour) over the core region. An east-west oriented cold front (within a weak trough) over the Black Sea lies between the high and the western-edge (1002 hPa contour) of the east-west oriented thermal Persian-Low, which has a westward projection north of the study area. The surface (warm core) Azores high and (cold core) frontal trough are both downward-extensions of 700 hPa features discussed above (as both intensify with height), while the (warm core) thermal Persian Low weakens with height and is thus not an extension of a 700 hPa feature.

Concurrent ECMWF pressures (Fig. 9a) capture the position and strength of the Azores high and its west-east projection (blue and grey areas) over the core area; weak cold-front trough over the Black Sea (grey blob); and east-west projection from the Persian Low (red and grey areas) north of the core area. Its concurrent winds over the study region (Fig. 10a) are dominated by both projections, i.e., counterclockwise in the northern part of the area from the Low (over Mediterranean Sea) and clockwise over the southern part of the domain from the high.

By 30 July (not shown), the front had dissipated, while the Persian Low strengthened and grew westward, which narrowed the eastward projection from the high. The concurrent ECMWF pressures (not shown) captured these changes, which did not significantly change flow directions. During the next 24 h, the IMS Thermal-Low protrusion continued to expand westward (Fig. 8b), while the High-protrusion retreated. ECMWF pressures (Fig. 9b) correctly captured both movements, but surface flows over the

southeastern part of the area had changed from anticyclonic/northerly to northwesterly as the high-protrusion retreated (Fig. 10b).

By 1 August at 0000 UTC (Fig. 8c), the IMS chart shows a new weak low north of the Black Sea. The high has weakened, but its southern protrusion and that from the Persian Low were mostly unchanged. The concurrent ECMWF (Fig. 9c) chart correctly shows these features, as well as a continued rotation (to westerly) of the winds in the southeastern part of the domain (Fig. 10c). By 2 August at 0000UTC, the northern IMS low (Fig. 8d) moved southward, the Persian Low protrusion started to retreat back east-ward, and thus the Azores protrusion could then push eastward. Concurrent ECMWF pressures (Fig. 9d) again showed the same changes, while surface winds (Fig. 10d) over Egypt showed a slight shift from the previous northwesterly to a now northeasterly direc-tion, as the high moved northward.

In summary, IMS 700 hPa charts showed that a low north of study region (over the Black Sea) split the eastern-end of the Azores High into eastern and western parts. The low first strengthened and moved southward over the core region, while at the end of the period it weakened and moved back northwards. Concurrent IMS surface charts showed a downward extension to the surface of the High, as well as a projection eastward (from its center) over the core area. They also showed a shallow thermal Persian Low trough and its westward projection north of the core area. This surface-low projection first strengthened and moved further westward, which caused the high-projection to re-treat back towards the west, a situation that reversed during the last day of the period. Corresponding ECMWF charts (which provide IC and BCs for MM5) reproduced all

14

these movements, while their surface flow patterns showed the area generally dominated by cyclonic flow from the Persian Low, except in its southwestern quadrant with its anti-cyclonic flow from the High.

While ECMWF outputs can thus provide large-scale BC forcing for MM5 that correctly reproduces the main GC/synoptic pressure-centers on the IMS observational charts, MM5 can refine these patterns and capture additional mesoscale coastal and topographic features. Outputs from its coarsest-domain thus focus (in additional detail, as its grid has a finer resolution than the ECMWF model) on 700 hPa and surface synoptic features, while those from its inner two domains focus on surface mesoscale transport-patterns.

MM5 Run-3 outer-domain 700 hPa patterns on 29 July at 0000 UTC (Fig. 11a) can only show (as a sub-section of the ECMWF domain) the southwest segment of the ECMWF/IMS Azores high (centered off-domain, to the west). The eastern part of this high is east of this domain, while their low is to its north. MM5 winds are correctly westerly off of the eastern Mediterranean and counterclockwise (versus observed northwesterly) around the high. The variable wind directions across the southern edge of the domain reflect influences of the protrusion from the southern lobe of the Azores (located southeast of the domain). Concurrent MM5 surface results (Fig. 11b) correctly reproduce the position and strength of the low over Cyprus and of the protrusion from the southern lobe of the Azores High across southern Israel into the West Bank and Jordan.

Two days later, on 31 July at 0000 UTC (Fig. 12a), the MM5 700 hPa pattern shows a small (unobserved) transitory high over Jordan and an anticyclonic northwesterly

flow from the eastern Mediterranean into the Sinai in association with the Azores High in the southeastern part of the domain; the protrusion from this high is now east of this domain. The concurrent surface pattern (Fig. 12b) correctly shows that the thermal-low protrusion expanded southward and westward (to combine with the Cyprus low), while the protrusion from the Azores High is correctly shown to have weakened and retreated westward.

By 1 August at 0000 UTC (high O_3 period), the 700 hPa transitory high has dissipated, while the low is correctly shown to have moved southward into the domain (Fig. 13a), bringing counterclockwise flow. The westward retreat of the Azores high (now off domain) has continued, and thus a similar retreat of its eastward protrusion into the southeastern part of the domain produced clockwise flow. The concurrent surface pattern (Fig. 13b) correctly shows the continued westward growth of the Persian Low and the thus continued weakening and westward retreat of the Azores High protrusion.

After 24 h, the 700 hPa synoptic low (Fig. 14a) has not retreated back to the north (as observed), while the Azores High protrusion (in southeastern corner of domain) has erroneously weakened, despite this error. The concurrent MM5 surface pattern (Fig. 14b), however, correctly shows the now weakening and eastward retreating Persian thermal-low and the associated strengthening of the Azores High protrusion.

In summary, MM5 outer-domain 700 hPa patterns correctly showed the southwest segment of the observed Azores high. Its eastward-directed protrusion also correctly first retreated due to the southward expansion of a low-pressure system into the domain. While by the end of the period, the MM5 synoptic low did not retreat northward (as ob-

16

served), its Azores-protrusion did correctly strengthen and move northward. Concurrent MM5 surface-patterns correctly showed both the low over Cyprus and surface 'footprint" of the Azores High protrusion. It also correctly showed the Persian Low protrusion, which expanded westward to combine with the Cyprus low and which thus caused the Azores High protrusion to retreat westward. By the end of the period, this protrusion correctly strengthened in association with the weakening surface Persian Low. As the surface Persian trough was north of the study area (and not over it), surface O_3 concentrations did not approach episode levels.

Daytime 1200 UTC (Fig. 15a) rawinsonde data showed weak warming (from 28 to 30^0C) of near-surface temperatures over the period. A super-adiabatic SBL formed during each daytime period, which at a depth of 125 m, was somewhat deep due to the extensive regional solar surface-heating. This layer was caped by a near neutral-stability PBL, whose temperatures decreased at close to the dry adiabatic rate (10^0C/km) until the base of the elevated subsidence inversion layer (thus located at the level of min temperature) associated with Azores High subsidence.

Nighttime 0000 UTC (Fig. 15b) surface rawinsonde-temperatures, however, showed no trend, with values between 23 and 26^0C over the period. The nightly 150 m nocturnal surface-based radiative inversion was relatively shallow due to the slow nocturnal release from the surface of the stored daytime solar-energy. This layer was also caped by a near-neutral PBL.

While the vertical time-height cross section (constructed from the 0000 and 1200 UTC soundings) cannot show all of the near-surface details discussed above (Fig. 16), it

does show that the elevated inversion-base height increased with time from 1000 m on 29 July 0000 UTC to 1600 m by 2 August 1200 UTC. The increase occurred as the surface Persian-trough pushed westward, producing the above discussed westward retreat of the Azores high and thus reducing subsidence. Minimum-temperatures at the base decreased with time during this period, as adiabatic cooling thus extended over an ever-deepening sub-inversion layer. The base began to lower at the end of the period, as the Azores high started to move back eastward. The deepening sub-inversion layer is another reason why O_3 levels did not reach episode levels during the study period.

b. MM5 statistical evaluation

This section compares observed and Domain-2 MM5 temperatures (at 2 m) and winds (at 10 m), as this domain contains all the IMS met observational sites. As thermally-driven meso-met flows are best modeled by accurately simulated PBL temperatures (Bornstein *et al.* 1996), the first comparisons will involve temperature.

Domain-average observed and MM5 results during the final three days (centered on the highest O_3 day) of all three simulations show expected smooth diurnal 2 m temperature-waves (Fig. 17). The observations first show slight decreases (0.5^0C) in daytime-max and nighttime min temperatures from 31 July to 1 August and then an even slighter increase (0.25^0C) on the next day. These changes arose from an initially increased and then decreased subsidence-induced heating, as the 700 hPa Azores high first moved into and then out of the study area. Without the use of analysis nudging, none of the three MM5 simulations was able to capture such small effects.

Run-1 underestimated daytime max values by about 1.2, 0.9, and 0.1°C for the three days, respectively, while it overestimated corresponding nighttime min values by about 1.2, 1.0, and 0.5°C. In addition, the simulation produced a too-rapid daytime cooling, which resulted in a daytime time-lead in its temperatures. The overestimated nighttime min temperatures were probably due to a too-large input lower BC deep soil temperature, which in set in MM5 as the average of the input ECMWF surface-temperatures for the simulation period. This procedure, however, fails to account for the increased with depth time-lag (order of several months at 1 m, Arya 1988), which thus produces too high MM5 summertime deep-soil BC temperatures.

To solve the nighttime problem, BC deep soil temperature must be lowered by an amount several times larger than the model-produced bias (Boucouvala *et al.* 2003). As the current nighttime Run-1 min-temperature bias averaged 1.5 K, Run 2 deep-soil BC temperature was reduced (by trial and error) by 9 K from the value used in Run-1. While Run-2 results showed significantly reduced biases during the first two nights, an over-correction (of about 0.5 K) occurred during the third night. In the Los Angeles study by Boucouvala *et al.* 2003, it was necessary to lower BC deep-soil temperature by only twice the original bias. In the current study, however, it was necessary to lower it by three times that amount, probably due to the extreme dryness (and hence low soil conductivity) of the area.

Daytime MM5 Runs-1 and 2 max temperatures were underestimated on the first two days because of a too-high input IC soil moisture content, which produced a too-large atmospheric latent heat-flux and hence a too-small sensible heat-flux. Lowering

19

this parameter to a more reasonable value (e.g., to account for drought conditions) can solve this problem (Jacobson 1999). IC soil moisture content is specified as a function of LU in the MM5 input table, along with other surface thermal and radiative parameters. Run-3 was thus carried out with the new deep soil BC from Run 2 and with a 10% limit on input IC soil moisture values for all area LU-types, whereas original non-water values ranged up to 50% (for irrigated crops). This low value is reasonable for Israel, given its dry climate and its efficient drip-irrigation practices. Results showed no change in the already correct max daytime temperature on the third day, and while the bias was totally eliminated for the second-day max value, it was only half corrected for the corresponding first day value.

Both the observed and Domain-2 MM5 10 m wind-speeds for all three simulations (Fig. 18a) showed expected diurnal variations, with higher daytime (about 5 m s^{-1}) than nighttime (1.5 m s^{-1}) speeds. All three simulations overpredicted nighttime min speeds during all four nights, but by < 0.5 m s^{-1}. While this is a small absolute-bias (and smaller than that from many other nighttime MM5 results), it is a relative-bias of about 33 % and it generally increased from Run-1 to 2 to 3.

Runs-1 and 2 produced similar daytime max speeds, with the underpredictions on the first two days (0.5 and 1.3 m s^{-1}, respectively) smaller than the overprediction on the third day (0.2 m s^{-1}). Run-3 max speeds were correct on Day-1 (except for a small under-predicted second-afternoon peak), improved on Day-2 (only underestimated by 0.7 m s^{-1}), but even more overpredicted (now by 0.6 m s^{-1}) on Day-3. These final biases are likewise smaller than those from many other daytime MM5 results.

Run 3 also produced the most accurate wind directions (Fig. 18b), which generally show daytime westerly (combined sea breeze and upslope) and nighttime south-southwesterly (combined land and downslope) flows on all three days. All runs showed a phase error throughout 31 July and during the latter part of 2 August. Run 3 wind directions were the most accuate during all three nights, while Run-1 directions were the worst. During all nighttime min-speed periods, the observed winds generally became southerly (180 deg) some time between 0500 to 0900 LST. Concurrent nighttime MM5 winds for all three simulations were out of phase (either leading or lagging) this southerly flow by several hours for all three nights. Results, however, genrally improved from Run 1 to Run 3, e.g., third-night directions during Runs-1, 2, and 3 reached 210 (worst), 200, and 190 (best) deg, respeectively.

During all three daytime max-speed periods, observed winds generally became westerly to northwesterly (about 275 deg) sometime after 0300 LST, while concurrent day-time MM5 winds generally showed no improvement from Run 1 to Run 3. During the first day, while directions did reach the observed 280 deg, they did so several hours too early. Second-day timing was improved, but the flow rotated beyond the observed 275 deg direction by about 15 deg, while during the final day the flow rotated beyond the same observed direction by about 25 deg.

In summary, as Run 3 produced min differences between observed and predicted met variables, they will be further dissussed in the following section. Its diurnal temperature and wind patterns will then be related to sea/land and mountain/valley circulation impacts on O_3 transport patterns.

c. Domain-3 winds

Modeled Domain-3 nighttime surface winds at 0300 LST (0000 UTC) on Aug 1 (Fig. 19a) showed a confluence zone (located slightly off-shore) that arose from the meeting of the on-shore westerly-directed background flow and the off-shore southerly-directed downslope flow from the narrow coastal plain. While these latter flows developed on both hills, they were strongest off of the eastern-facing slopes, where they were in the same westerly-direction as the background flow. The inland directed flows north and south of both hills resulted as stable PBL flows tends to go around (and not over) obstacles. The downslope flows between the hills converged to form a locally-induced inland-directed westward channel-flow towards Jerusalem, unconnected (Fig. 19b) to the same-direction onshore flow over the Mediterranean (Fig. 19a).

The convergence zone continued to move offshore until 0900 LST (Fig. 20a), after which it started to move back onshore. By this time, the down-slope flow had been mainly replaced by upslope flows, which cannot be seen on the east-facing slope of the northern hill, as it is too close to the domain-edge. The channel flow towards Jerusalem (Fig.20b) is now less convergent than before. By 1000 LST (not shown), an on-shore sea breeze has formed in the northern half of the coastal plain.

By 1100 LST (Fig. 21a), the sea breeze had developed all along the coastal plain and upslope flows had developed on both sides of both hills, with a coastal-plain near-calm zone separating the westerly-directed upslope (on western slopes) and sea breeze flows; this separation shows the unique origin of each of these flows. During this daytime unstable PBL period, flows tends to go over (and not around) obstacles (Fig. 21b),

22

and thus the flow to Jerusalem is pure westerly and not convergent as it had been during the previous nighttime period.

By 1300 LST, the sea breeze had penetrated far enough inland to have merged with the western-side upslope flow (Fig. 22a, b). The combined strong westerly-flow penetrates over both hilltops and thus prevents east-side upslope flows from reaching either peak. By 1600 LST (Fig. 23a), a narrow-stream of westerly sea breeze air is drawn southeastward (as a northwesterly flow) towards the western sides of both heated hills, and upslope-flow on west-facing slopes is completely absent (Fig. 23b).

Sea breeze flows remained over the entire domain during the next few hours, but turned northwesterly by 2000 LST (Fig. 24a, b). During the following few hours (not shown), the coastal-plain flows weakened, sea breeze flows continued east of both hill-tops, and down slope flows had not yet formed. By 2300 LST (Fig. 25a), coastal-plain flows are offshore, due to nocturnal down-slope easterly-flows from the western-face of the (taller and more coastal) southern hill. Down-slope flows from both east-facing slopes are strong because of the prevailing northwesterly background flow, and converg-ent flow contributes to channeling towards Jerusalem (Fig. 25b). As the night progressed (not shown), down slope flows strengthened and thus again produced offshore flows over the entire coastal plain.

In summary, MM5 Domain-3 surface flow patterns simulated the expected di-urnal variation of the thermally-driven coastal and slope flows expected in coastal Israel on 1 August 1997. Results from the other days in the study period were not shown, as

they were similar to those presented. The following section describes the observed surface flow and O_3 tranpsort patterns.

d. Observed surface O_3-transport

At 0300 LST (0000 UTC) on 1 August (Fig. 26a), observed nighttime surface winds were mostly offshore, i.e., easterly or southeasterly over the narrow coastal plain region and westerly off the eastern side of the Haifa peninsula. This nocturnal offshore flow was also captured in the MM5 Domain-3 results in Fig. 17a. It results when the combined land breeze and down-slope flows (off the west-facing slopes) are strong enough to over-come the prevailing onshore/westerly large-scale flow from the southern edge of the (now weakened) thermal Persian Low (Fig. 13b).

The westerly flow at inland sites (east of coastal ridge) results from combined canyon channeling of the large-scale and down-slope (off east-facing slopes) flows, e.g., to Jerusalem/Modiin. Speeds range up to 4 m s^{-1} and expected low nocturnal O_3 values (<40 ppb) are found over most of the region, except over the Haifa urban/industrial area, where values are still 51 ppb.

Little changed during the next five hours, but at 0900 LST (Fig. 26b) the observed winds reversed and strengthened (to 6 m s^{-1}). The flow was thus mostly onshore/southwesterly and again shows local channeling westward to Jerusalem/Modiin. This night-day reversal, due to development of combined daytime sea breeze and upslope flows that augment the prevailing onshore large-scale flow from the Persian Low, is not yet seen in the concurrent MM5 Domain-3 results (Fig. 18a). Expected higher morning O_3 values are found downwind (i.e., 20 km inland) of the less-urban regions between Haifa and Tel

Aviv (66 ppb at Maapil) and southeast of Tel Aviv (58 ppb at Modiin); no observations are available at the similar areas north of Haifa. Lower values are seen at the coastal urban sites in Tel Aviv (46 ppb) and Haifa (40 ppb).

By 1100 LST (Fig. 26c), speeds had increased to 7 m s^{-1}. While coastal directions were mostly unchanged, they were reversed to easterly at a few inland-sites, i.e., up-slope on the east-facing sides of the inland hills. The concurrent MM5 Domain-3 results (Fig. 19a) now does show the correct coastal onshore flow-direction. The daily O$_3$-peak (72 ppb) was reached at this time at Maapil, while a secondary max occurred at Modiin (66 ppb). By noon (not shown), speeds were unchanged and max O$_3$ values (still over Maapil) decreased to 66 ppb.

Directions during the next four hours (up to 1600 LST) at inland-sites remained upslope. Coastal winds, however, changed from their previously southwesterly direction to become mostly westerly (Fig. 26d), as also seen in the MM5 Domain-3 results (Fig. 21a). The change resulted from the concurrent eastward growth of the surface protrusion from the Azores High (Figs. 13b versus 14b). Maapil O$_3$ levels were reduced to 61 ppb, with a secondary max of 54 ppb at Modiin and Ashkelon (north of Gaza Strip). Coastal winds were still westerly at 1700 LST (not shown), except at sites south of Tel Aviv, where they had changed to northwesterly; speeds still ranged from 5-7 m s^{-1} over the entire area.

By 2000 LST (Fig. 26e), observed directions had become northwesterly over the southern part of the area, as captured in the MM5 results (Fig. 22a), which show a northwesterly 700 hPa prevailing flow. While coastal speeds had decreased to 3 m s^{-1} as the

onshore (sea breeze and upslope) flows weakened, those at some northern inland-sites remain high at 6 m s^{-1}. Max O$_3$ values continued to decrease, but were still 53 ppb at Mappil, 51 ppb at Ashkelon, and 45 ppb at Modiin. After three hours (Fig. 26f), down slope flows had formed at inland sites, and while most coastal O$_3$ values had dropped to about 30 ppb, they remained somewhat higher at Haifa (41 ppb).

This summer non-episode day (Fig. 27a) shows max surface O$_3$ values at 1100 LST at Maapil (20 km inland), where values remained relatively high (~63 ppb) until 1900 LST. Values were minimum during all daytime hours (at ~37 ppb) at coastal urbanized Newe Shaanan and likewise moderate (~43 ppb) at coastal non-urbanized Ashdod YA. Ozone at these sites results from photochemical production from precursors from coastal surface-transportation sources, with lower urban values due to NO$_x$ titration of O$_3$. During the preceding night, the concentration ranking had been reversed, with max O$_3$ at the highest elevation site (Newe Shaanan) and min O$_3$ at the lowest elevation site (Ashdod YA). The reversal could be associated with nocturnal down-slope flows, which recirculate high-O$_3$ daytime-air back over the coastal plain (Fernando 2006).

While the time of the Jerusalem peak appears several hours earlier than found at other sites around the world, simulations by WEIN05 have shown a larger (and later) peak over western Jordan (east of current domain). This later peak arises due to the slowness of the photochemical processes that act on more substantial precursor emissions from a large coastal power plant.

On 2 August at 0300 LST (Fig. 28a), observed nighttime surface winds were again (as on previous day) up to 4 m s^{-1} and offshore over both the coastal-plain and

26

eastern Haifa peninsula. Westerly flow at inland sites again resulted from combined canyon channeling to Jerusalem/Modiin of the large-scale and down-slope flows. Ozone values, however, are generally lower (mostly <40 ppb) than the previous night, with a max again near urban-Haifa (47 ppb at Nesher). By 0900 LST (Fig.28b), winds again reverse to on-shore/southwesterly and speeds again strengthen to 5 m s^{-1}. Higher O_3 values are also again found downwind of the less-urban regions between Haifa and Tel Aviv (again 66 ppb at Maapil) and southeast of Tel Aviv (57 ppb at Modiin), with lower values again at coastal-urban sites in Tel Aviv (42 ppb) and Haifa (45 ppb).

By 1100 LST (Fig. 28c), speeds had again increased to 6 m s^{-1}. While coastal directions were again mostly unchanged, a few inland directions again reversed to easterly/ upslope. The daily O_3-peak (70 versus 72 ppb for 1 August) was again at Maapil, while the secondary max was gain at Modiin (60 ppb). Flow directions again remained generally southwesterly for the next five hours, when coastal winds became westerly by 1600 LST (Fig. 28d), as the Azores High protrusion now strengthened. A few inland winds were still upslope, and Maapil O_3 levels again reduced to 59 ppb.

By 2000 LST (Fig. 28e), coastal speeds again decreased (~3 m s^{-1}) and relatively high O_3 was again still found at Mappil (46 ppb) and Modiin (40 ppb), while Gaza again shows 51 ppb (as on previous day). Three hours later, winds were still onshore/westerly at both coastal and inland sites (Fig. 28f), while O_3 again had generally dropped to 30 ppb, but remained at 43 ppb at Modiin.

As the winds on 2 August were similar to those on the previous day, its diurnal O_3 variations (Fig. 27b) again show an 1100 LST O_3 max at inland Maapil. Values at Maa-

pil again remained relatively high (about 63 ppb) until 1900 LST, as compared to those at coastal urbanized Newe Shaanan (about 40 ppb) and coastal non-urbanized Ashdod YA (about 45 ppb).

4. Conclusion

Large-scale and mesoscale summertime met-conditions over the West Bank, Gaza Strip, and Israel during 29 July to 3 August 1997 were studied, with a focus on surface O_3 transport-patterns on 1 and 2 August. The period was selected because HUJI airborne observations at 300m showed near-episode O_3 concentrations above Jerusalem, although only average-summertime non-episode surface-O_3 conditions existed. In addition, a relatively dense surface observational meso-met network was operational, and the episode had been previously modeled at the HUJI by use of linked meso-met and photochemical models.

IMS observed met-data and weather charts were first analyzed to better understand both the large-scale upper level and surface flow patterns. A series of three MM5 simulations were then carried out on three (two-way) nested domains, closely matched to those of the HUJI RAMS simulations. The new simulations used a min grid-spacing of 1.67 km, 1.5 level TKE, and ECMWF large-scale IC and BC fields, but did not use either observational or analysis nudging.

The IMS charts showed the large-scale 700 hPa flow pattern dominated by interactions between the upper level projection of the eastern edge of the Azores High and a low-pressure center north of the study area, while those at the surface involved the Azores High and the shallow surface Persian Low thermal-trough. The upper level charts showed that the low center first strengthened and moved southward over the core region, which further split the eastern and western parts of the Azores High.

Concurrent IMS surface charts showed a projection eastward from the Azores High over the core area. They also showed that the Persian Low had a westward projection north of the core area, which first strengthened and moved further westward, which caused the high-projection to re-treat back towards the west. Corresponding ECMWF input into MM5 reproduced all these movements. It also showed surface flow patterns generally dominated by cyclonic flow from the Persian Low, except in the southwestern quadrant of the domain, which showed anti-cyclonic flow from the High.

Predicted domain-averaged surface temperatures, wind speeds, and wind directions were compared against the IMS observations. Minimum MM5 biases resulted in nighttime/max and daytime/min temperatures when its input deep-soil BC temperature was lowered by 9°C in combination with its IC soil moisture content being lowered to a max of 10%. These adjustments also produced min biases in wind speed and direction.

MM5 outer-domain 700 hPa patterns correctly showed the Azores High and its eastward-directed protrusion, which first retreated due to the southward expansion of a low-pressure system. Concurrent MM5 surface-patterns correctly showed the Azores High protrusion and the Persian Low protrusion, which expanded westward and caused the first protrusion to retreat westward. As the surface Persian trough was north of the study area (and not over it), surface O_3 concentrations did not approach episode levels during the study period.

MM5 inner domain surface flow patterns correctly reprodcued the observed diurnal variation of the thermally-driven summertime surface coastal and slope flows in the area. Nighttime flows were mostly offshore over the narrow coastal plain, due to com-

bined land breeze and down-slope flows strong enough to overcome the prevailing on-shore large-scale flow from the southern edge of the thermal Persian Low. Morning flows were mostly onshore with local channeling westward to Jerusalem, due to combined daytime sea breeze and upslope flows that augmented the prevailing onshore large-scale flow. Afternoon coastal winds become mostly westerly due to the concurrent eastward growth of the surface protrusion from the Azores High, while nighttime down slope flows again formed.

This summertime non-episode day showed max observed surface O_3 values at 1100 LST at a site 20 km inland from the coast, where values remained relatively high until 1900 LST. Values were minimum during daytime hours at coastal urbanized sites and likewise moderate at coastal non-urbanized sites. Ozone at these sites results from photochemical production from precursors from coastal surface-transportation sources, with the lower urban values due to NO_x titration of O_3.

While the time of the Jerusalem peak appears several hours earlier than found at other sites around the world, HUJI simulations have shown a larger (and later) peak over western Jordan (east of current domain). This later peak arises due to the slowness of the photochemical processes that act on more substantial precursor emissions from a large coastal power plant.

Future efforts should further improve the MM5 results by use of observational-nudging of temperature, wind velocity, and humidity. Current input surface roughness values in MM5 are too small for complex topographic regions, such as the current study area. Increases in these input values will decrease the currently somewhat overestimated

nighttime wind speeds. Finally, additional insight into surface and upper level ozone transport patterns in the region could be achieved if the current MM5 met results were used to drive Lagrangian-particle dispersion and/or photochemical air quality models.

REFERENCES

Alpert, P., B. Getenio, and R. Zak-Rosental, 1988: One-level modeling for diagnosing surface winds over complex terrain. Part II: Applicability to short-range forecasting. *Mon. Wea. Rev.*, **116**, 2047-2061.

Arritt, R. W., 1989: Numerical modeling of the offshore extent of sea breezes. *Quart. J. Roy. Meteor. Soc.*, **115**, 547-570.

Arya, 1988: *Introduction to Micrometeorology.* Academic Press, NYC, 307 pp.

Bornstein R., 2006: Simulation of mesoscale urban transport processes with numerical models: guidelines to accurate simulations. Presented at 14th Joint AMS AWMA Conf. on the Applications of Air Pollution Meteor., 29 Jan.-2 Feb., Atlanta, GA.

Boucouvala, D., R. Bornstein, J. Wilkinson, and D. Miller, 2003: MM5 simulations a SCOS97-NARSTO episode. *Atmos. Environ,* **37**, S95-S117.

Blackadar, A. K., 1957: Boundary layer wind maxima and their significance for the growth of nocturnal inversion. *Bull. Amer. Meteor. Soc.*, **38**, 283-290.

Clappier A. et al., 2000: Effect of sea breeze on air pollution in the Greater Athens Area. Part I: Numerical simulations and field observations. *J. Appl. Meteor.*, **39**, 546-62.

Dayan, U., R. Shenhav, and M. Graber, 1988: The spatial and temporal behavior of the mixed layer in Israel. *J. Appl. Meteor.*, **27**, 1382-1394.

Dayan, U. and L. Koch, 1996: Ozone concentration profiles in the Los Angeles Basin – A possible similarity in the build-up mechanism of inland surface ozone in Israel. *J. Appl. Meteor.*, **35**, 1085-1090.

Dayan, U., and I. Levy, 2002: Relationship between synoptic-scale atmospheric circulation and ozone concentrations over Israel. *J. Geophys. Res.*, **107**, 31-44.

Dayan, U., and J. Rodnizki, 1999: The Temporal Behavior of the Atmospheric Boundary Layer in Israel. *J. Appl. Meteor.*, **38**, 830-836.

Dean, R. O., V. Matveev, U. Dayan, M. Peleg, J. Kaplan, A. Gertler, M. Luria, G. Kallos, P. Katsafados, and Y. Mahrer, 2002: Impact of coastal transportation emissions on inland air pollution over Israel: Utilizing numerical simulations, airborne measurements, and synoptic analyses. *J. Geophys. Res.*, **107**, NO. 0,10.1029/2001JD000808.

Doron, E., and J. Neumann, 1977: Land and mountain breezes with special attention to Israel's Mediterranean coastal plain. *Israel Meteor. Res. Papers*, **1**, 109-122.

Dudhia, J., 1993: A nonhydrostatic version of the Penn-State-NCAR mesoscale model: validation tests and simulation of an Atlantic cyclone and cold front. *Mon. Wea. Rev.*, **121**, 1493-1513.

Dudhia, J., 2001: Mesoscale model nesting and boundary conditions. National Center for Atmospheric Research, Boulder, Colorado, USA [http://meteo.usc.es/ documents/jm.pdf].

Dudhia, J., and J. F. Bresch, 2002: A global version of the PSU-NCAR mesoscale model. *Mon. Wea. Rev.*, **130**, 2898-3007.

Dudhia, J., D. Gill, K. Manning, W. Wang, and C. Bruyene, 2003: PSU/NCAR Mesoscale Modeling System Tutorial Class Notes (MM5 modeling system version 3) [http://www.mmm.ucar.edu/mm5/ documents/tutorial-v3-notes.html].

Ellicott, A., 1799: Miscellaneous observations relative to the neighborhood of Lake Erie. *Amer. Philos. Soc. Trans.*, **4**, 224-229.

Fernando H., and K. Park, 2006: The use of an urban canopy parameterization for MM5 : Application to the Phoenix airshed. Presented at the AMS Sixth Symposium on the Urban Environment, 29 Jan-2 Feb, Atlanta, GA.

Gayno, G., 1994: Development of a higher-order, fog-producing boundary layer model suitable for use in numerical weather prediction. MS Thesis, Penn. State University, 104 pp.

Giovannoni J.M., A. Clappier, and A. Russell, 1995: Ozone control strategy modeling and evaluation for Athens, Greece: ROG vs. NOx effectiveness and the impact of using different wind-field preparation techniques. *Meteor. Atmos. Phys.*, **57**, 3-20.

Grell, G. A., J. Dudhia, and D. R. Stauffer, 1994: A description of the fifth-generation Penn State/ NCAR mesoscale model (MM5), *NCAR Technical Note, NCAR/TN-398+STR*, 117pp. [Available from NCAR Information Services, P.O. Box 3000, Boulder, CO 80307, USA].

Hashmonay R., A. Cohen, and U. Dayan, 1991: Lidar Observation of the Atmospheric Boundary Layer in Jerusalem. *J. Appl. Meteor.*, **30**, 1228-1236.

Hebestreit, K., J. Stutz, D. Rosen, V. Matveev, M. Peleg, M. Luria, and U. Platt, 1999: First DOAS measurements of tropospheric BrO in mid-latitudes. *Science,* **283**, 55-57.

Jacobson, M. Z., 1999: Effects of soil moisture on temperatures, winds, and pollutant on concentrations in Los Angeles. *J. Appl. Meteor.*, **38**, 607-616.

Kasakseh, S., R. Bornstein, and E. Weinroth, 2006: CAMx simulations of Middle-East ozone concentration-trends by use of RAMS and MM5 input. Presented at the AMS Eighth Conf. on Atmospheric Chemistry, 29 Jan.-2 Feb., Atlanta, GA.

Lu, R., M. Z. Jacobson, and R. P. Turco, 1997: An integrated air pollution modeling system for urban and regional scales: Part 1. Structure and performance. *J. Geophys. Res.*, **102**, 6063-6079.

Mahrt, L., 1981: The early evening boundary layer transition. *Quart. J. Roy. Meteor. Soc.*, **107**, 329-343.

Matveev, V., M. Luria, D. Alper-Siman Tov, and M. Peleg, 2002: Long-range transportation of air pollutants from Europe to Israel. *Isr. J. Earth Sci*, **51**, 17-28.

McNider, R., M. Moran, and R. Pielke, 1988: Influence of diurnal and inertial boundary layer oscillation on long-range dispersion. *Atmos. Environ.*, **11**, 2445-2462.

Neumann, J., 1951: Land breezes and nocturnal thunderstorms. *J. Meteorol.*, **8**, 60-67.

Neumann, J., and Y. Mahrer, 1971: A theoretical study of the sea and breeze circulation. *J. Atmos. Sci.*, **28**, 534-542.

Neumann, J., 1984: The Coriolis force in relation to the sea and land breezes: a historyical note. *Bull. Amer. Meteorol. Soc.*, **65**, 24-26.

Pielke R. A., W. R. Cotton, C. J. Tremback, W. A. Lyons, L. D. Grasso, M. E. Nicholls, M. D. Moran, D. A. Wesley, T. J. Lee, and J. H.Copeland, 1992: A comprehensive meteorological modeling system. *Meteor. and Atmo. Physics,* **49**, 69-91.

Peleg, M., M. Luria, I. Setter, D. Perner, and P. Russel, 1994: Ozone levels in central
Israel. *Israel J. Chem.*, **34**, 375-386.

Perlin, N., and P. Alpert, 2000: Effects of land-use modification on potential increase of
convection: A numerical mesoscale study over south Israel. *J. Geophys. Res.*, **106**,
22 621- 22 634.

Rotunno, R., 1983: On the linear theory of the land and sea breeze. *J. Atmos. Sci.*, **40**,
1999-2009.

Seinfeld J. H., and S. Pandis (Eds.), 1998: *Atmospheric Chemistry and Physics: Air Pol-
lution to Climate*. John Wiley & Sons, New York, 1326 pp.

Sillman S., D. Y. He, C. Cardelino, and R. E. Imhoff, 1997: The use of photochemical in-
dicators to evaluate ozone-NOx-hydrocarbon sensitivity: Case Studies from At-
lanta, New York, and Los Angeles. *J. Air and Waste Management Assoc.*, **47**,
1030-1040.

Svensson G., 1998: Model simulation of the quality in Athens, Greece, during the
Medcaphot-trace campaign. *Atmos. Environ.*, **32**, 2239-2268.

Walko R. L., C. J. Tremback, and M. J. Bell, 1995: HYPACT the Hybrid Particle and
Concentration Transport Model. *User's Guide Version 1.0*, Aster Division.

Weinroth E., 2005: Middle East Transboundary Pollutant Transport. Presented at
ASAAQ Conf., 24-28 April, San Francisco.

Yan H., and R. A. Anthes, 1987: The effect of latitude on the sea breeze. *Mon. Wea. Rev.*,
115, 936-956.

Ziomas I.C., P. Tzoumaka, D. Balis, D. Melas, C. Zerefos, and O. Klemm, 1998: Ozone

episodes in Athens Greece. A modeling approach using data from the

MEDCAPHOT-TRACE. *Atmos. Environ.*, **32**, 2313-2321.

Appendix A: ACRONYMS

BC	Boundary Condition
BSa	Koppen Semi-dry climate with hot summers
CAMx	Comprehensive Air Quality Model with extensions
Csa	Koppen mid-latitude dry-summer climate with cool summers
ECMWF	European Center for Medium-Range Weather Forecasts
GC	General Circulation
HUJI	Hebrew University Jerusalem Israel
HUJI97	HUJI 1997 field-study
IC	Initial Condition
IMS	Israeli Meteorological Service
LLJ	Low Level Jet
LST	Local Standard Time
LU	Land Use
MET	Meteorological
MM5	Fifth-generation Mesoscale Meteorological Model
NCAR	National Center for Atmospheric Research
PBL	Planetary Boundary Layer
PSU	Pennsylvania State University
RAMS	Regional Atmospheric Modeling System
SST	Sea Surface Temperature
TKE	Turbulent kinetic Energy
WEIN05	Weinroth 2005 modeling study

Appendix B: TABLES

Table 1: Observational meteorological network

Station No.	Station Name	Latitude (^{0}N)	Longitude (^{0}E)
1	Ben-Dor	32.80	35.00
2	Haifa	32.82	35.00
3	Katzir	32.49	35.10
4	Ta1	32.11	34.79
5	Bitzron	31.79	34.73
6	Ta2	32.04	34.78
7	Ramat-Sharon10m	32.14	34.84
8	Yavne	31.87	34.74
9	Kfar-Shmoel	31.88	34.93
10	Dovrat	32.65	35.35
11	Tavor	32.68	35.42
12	Haifa2	32.78	35.04
13	Beit Eliezer	32.43	34.92
14	Hadera	32.43	34.89
15	Orakiva	32.50	34.92
16	Netanya	32.33	34.86
17	Elyakim	32.63	35.07
18	Zichron	32.57	34.95
19	Pardes Hana	32.47	34.97
20	Elyachin	32.40	34.93
21	Menashe	32.60	35.05
22	Givat Ada	32.52	35.01
23	Maagan Michael	32.55	34.91
24	Hamaapil	32.37	34.98
25	Magal	32.38	35.04
26	Kerem Mah	32.64	34.99
27	Dalya Alk	32.69	35.04
28	K. Ata	32.81	35.10
29	Newe S.	32.79	35.00
30	Nesher	32.77	35.04
31	Modiin	31.90	35.02
32	Ashkelon	31.67	34.56
33	K. Gat	31.61	34.77
34	Yavniel	32.70	35.51
35	Tavor	32.71	35.41
36	Gilboaa	32.55	35.39
37	Ariel	32.11	35.18
38	Jerusalem	31.78	35.22
39	Shani	31.36	35.07
40	Gilgal	32.00	35.45

41	Hatseva	30.78	35.24
42	Faran	30.37	35.16
43	Haifa3	32.76	35.02
44	Techinion	32.77	35.02
45	Ein Carmel	32.77	35.02
46	Ein Hashophet	32.60	35.09
47	Zicron	32.57	34.95
48	Hadera	32.47	34.88
49	Bit Dagan	32.01	34.81
50	Bsor	31.27	34.39
51	Beersheva	31.25	34.80
52	Sedeboker	30.85	34.78
53	Sdom	31.03	35.39
54	Avnaitan	32.82	35.76
55	Btche	32.88	35.65
56	Tsmch	32.70	35.58
57	Nremmek	32.60	35.28
58	Hvteden	32.47	35.49

Table 2: Observational O_3 network

Station No.	Station Name	Latitude (^{0}N)	Longitude (^{0}E)
1	Kiryat Ata	32.81	35.10
2	Newe Shaanan	32.79	35.00
3	Nesher	32.77	35.04
4	Maapil	32.38	34.98
5	Cent. Station	32.06	34.78
6	Antokolski	32.10	34.80
7	Fire Dept.	32.08	34.82
8	Yavne Group	31.87	34.74
9	Oil Site	31.15	34.82
10	Modiin	31.90	35.02
11	Ashdod	31.80	34.64
12	Gedera	31.82	34.78
13	Ashdod YA	31.78	34.62
14	Ashdod Y	31.78	34.66
15	Ashkelon	31.67	34.56
16	Kiryat Gat	31.61	34.77
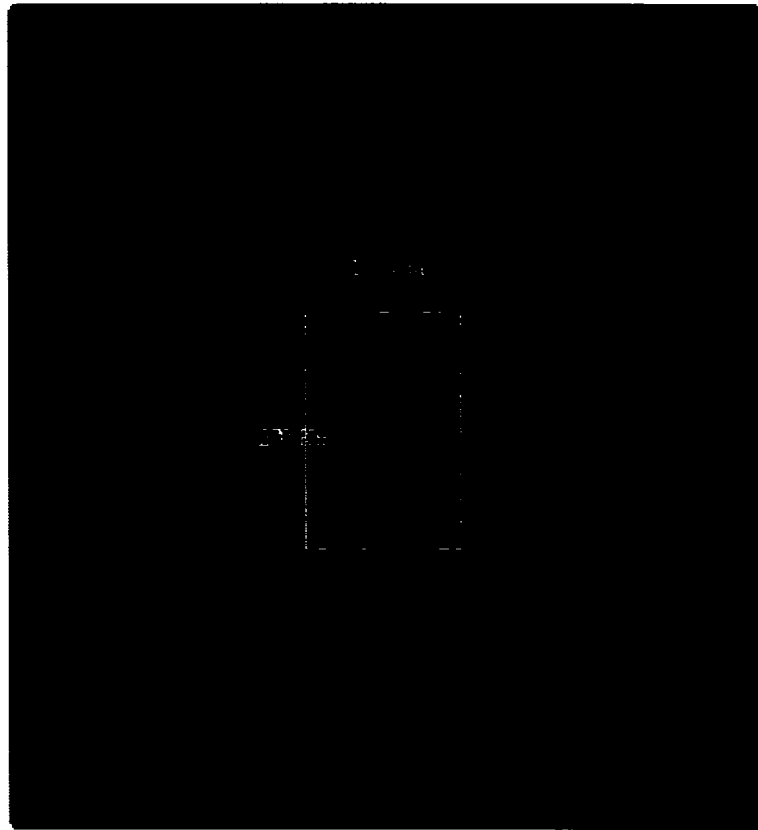
Fig. 1. Three RAMS domains, with 900 by 900 km coarsest domain
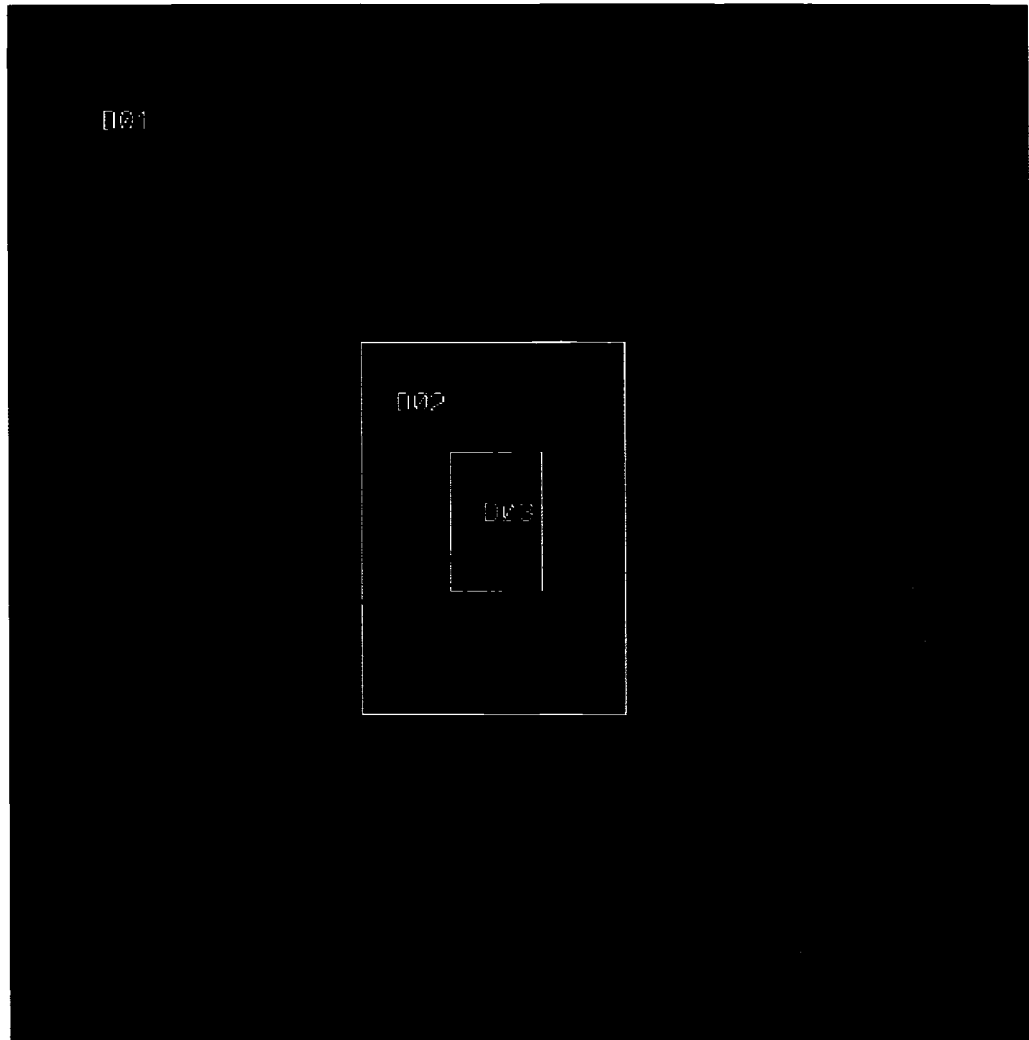
Fig. 2. Three MM5 domains
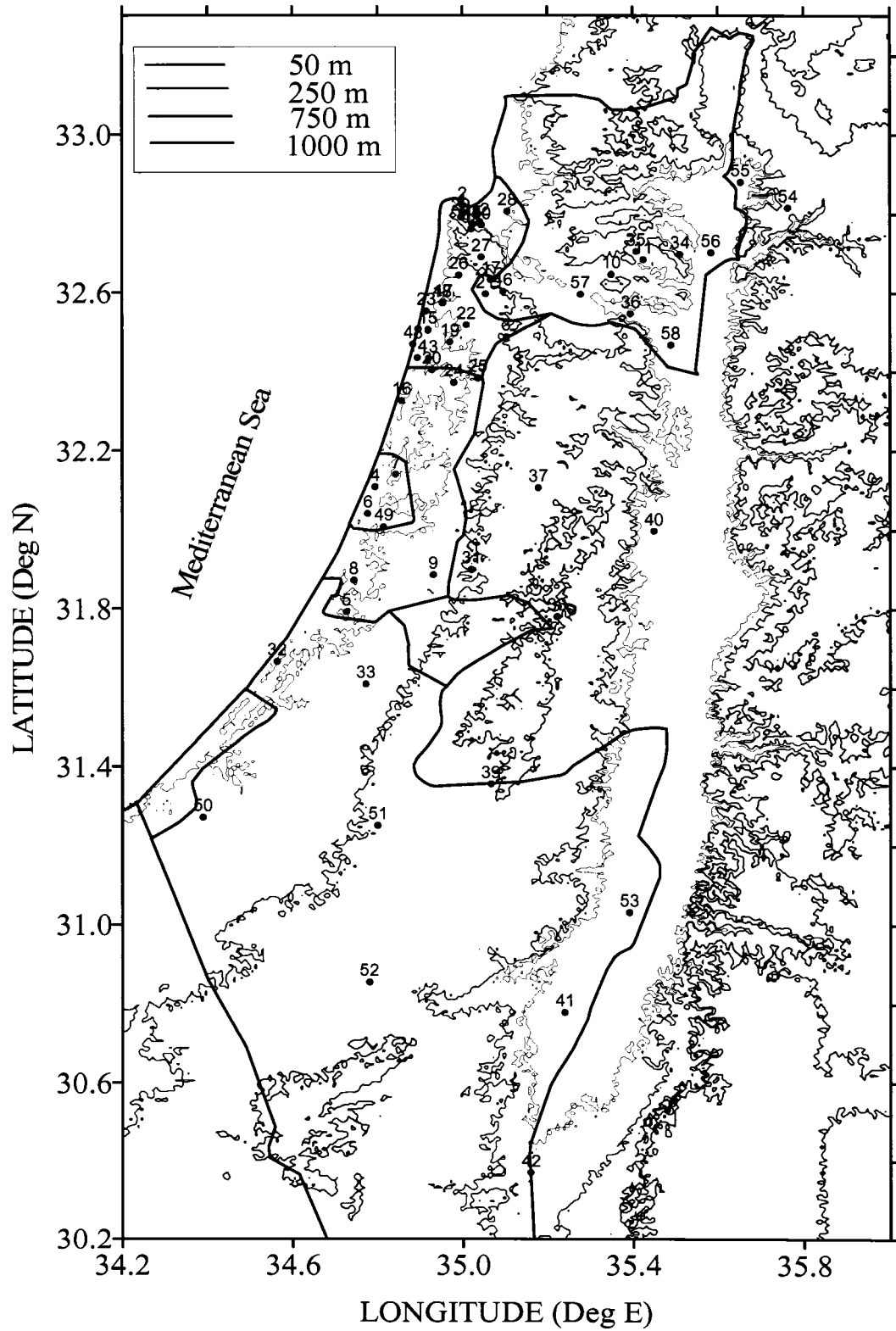
Fig. 3. Meteorology observational sites (see Table 1 for names), with key topographic heights (m)
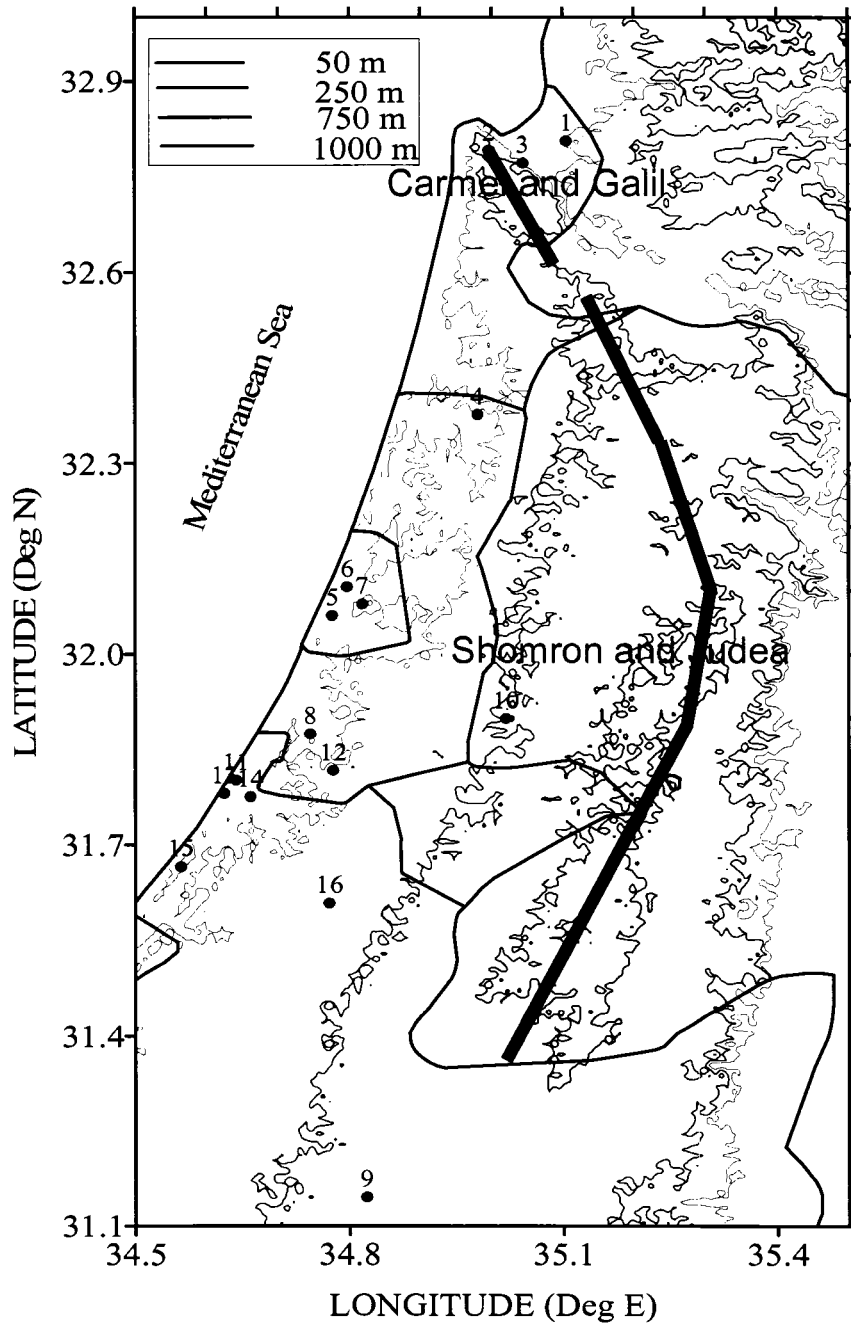
Fig. 4. O₃ observational sites (see Table 2 for names), key topographic heights (m), and named hills with ridge-lines
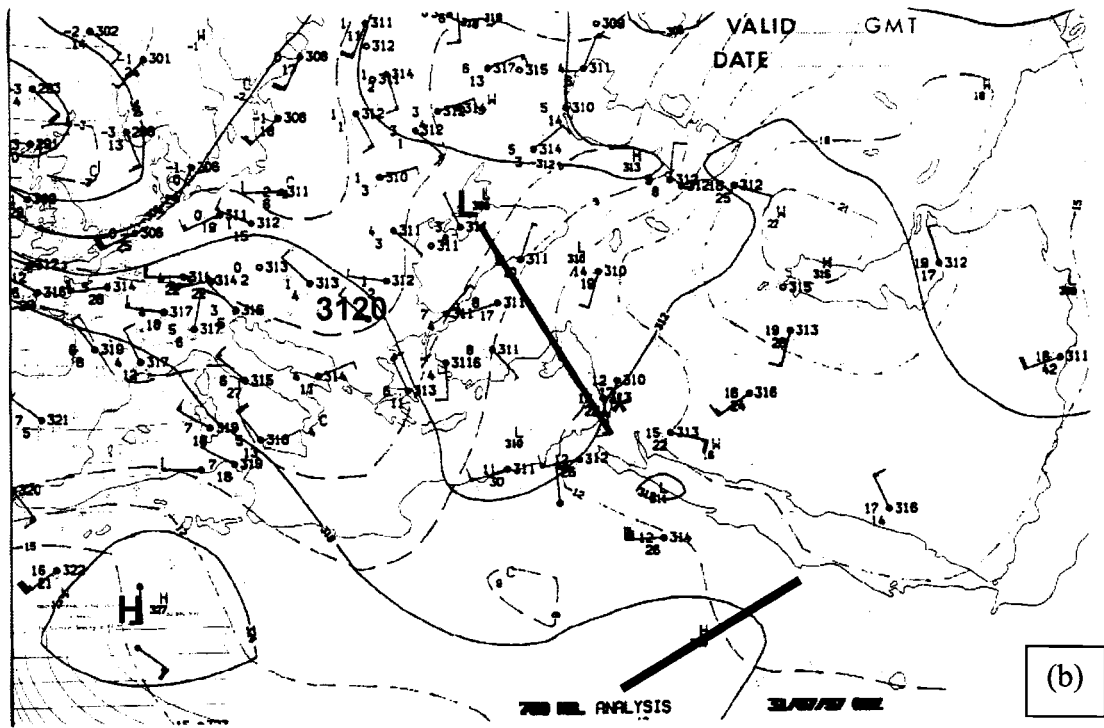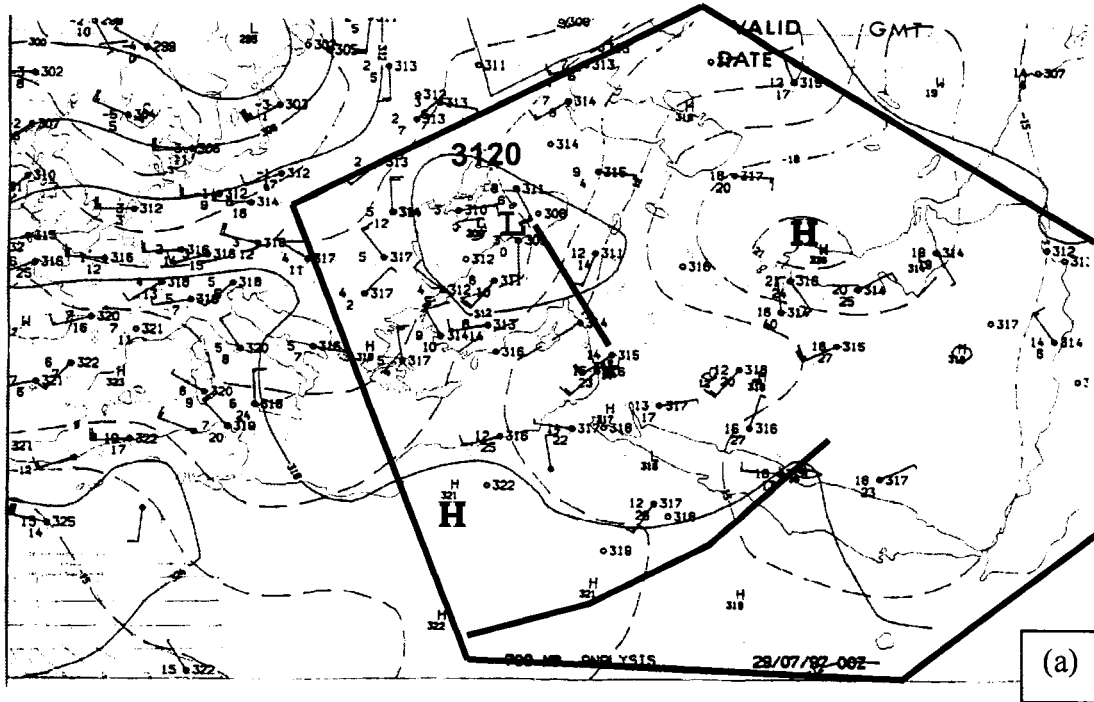
Fig. 5. 1997 IMS 700 hPa heights (dm) at 0000 UTC (where asterisk marks study-area and box marks ECMWF domain) on: (a) 29 July and (b) 31 July
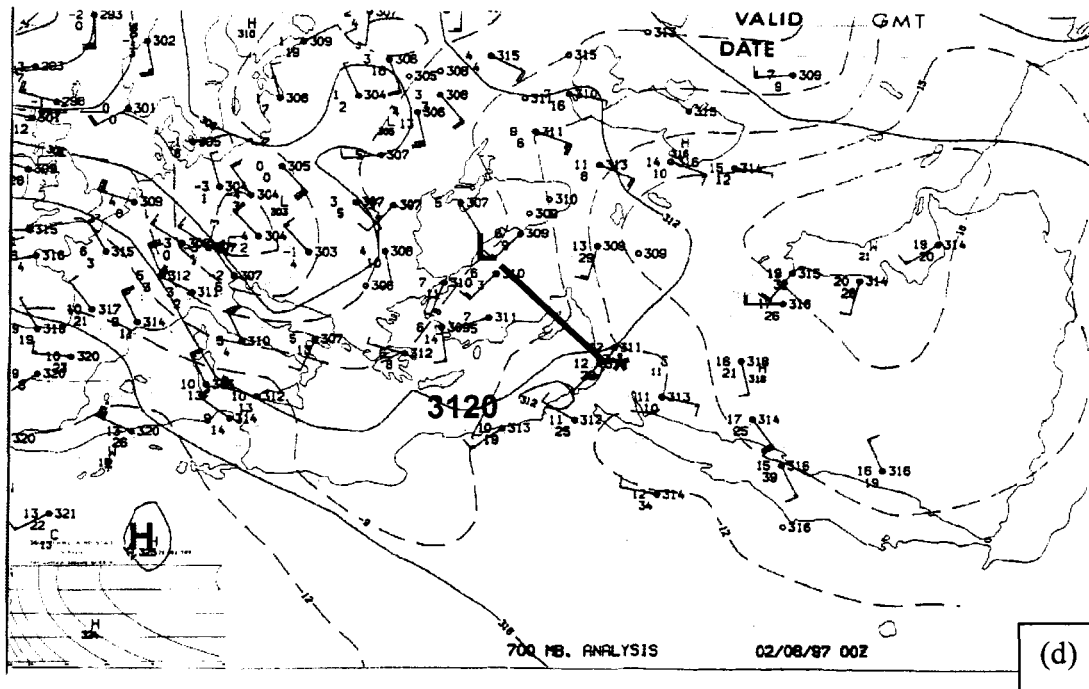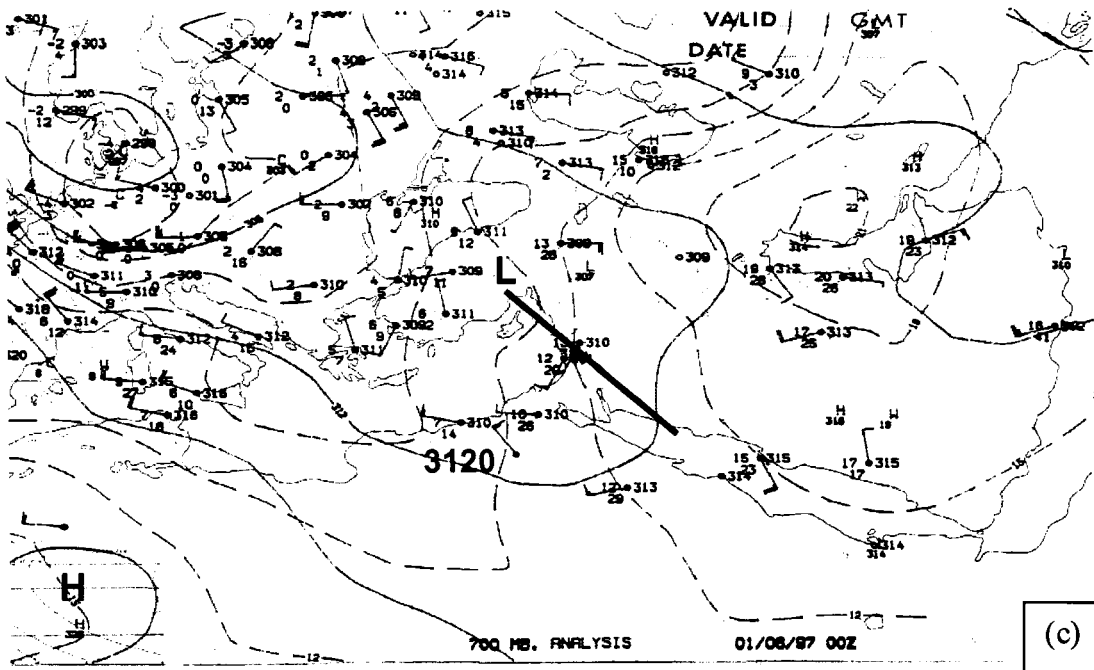
Fig. 5. 1997 IMS 700 hPa heights (dm) at 0000 UTC (where asterisk marks study-area center) on (c) 1 August (d) 2 August

48
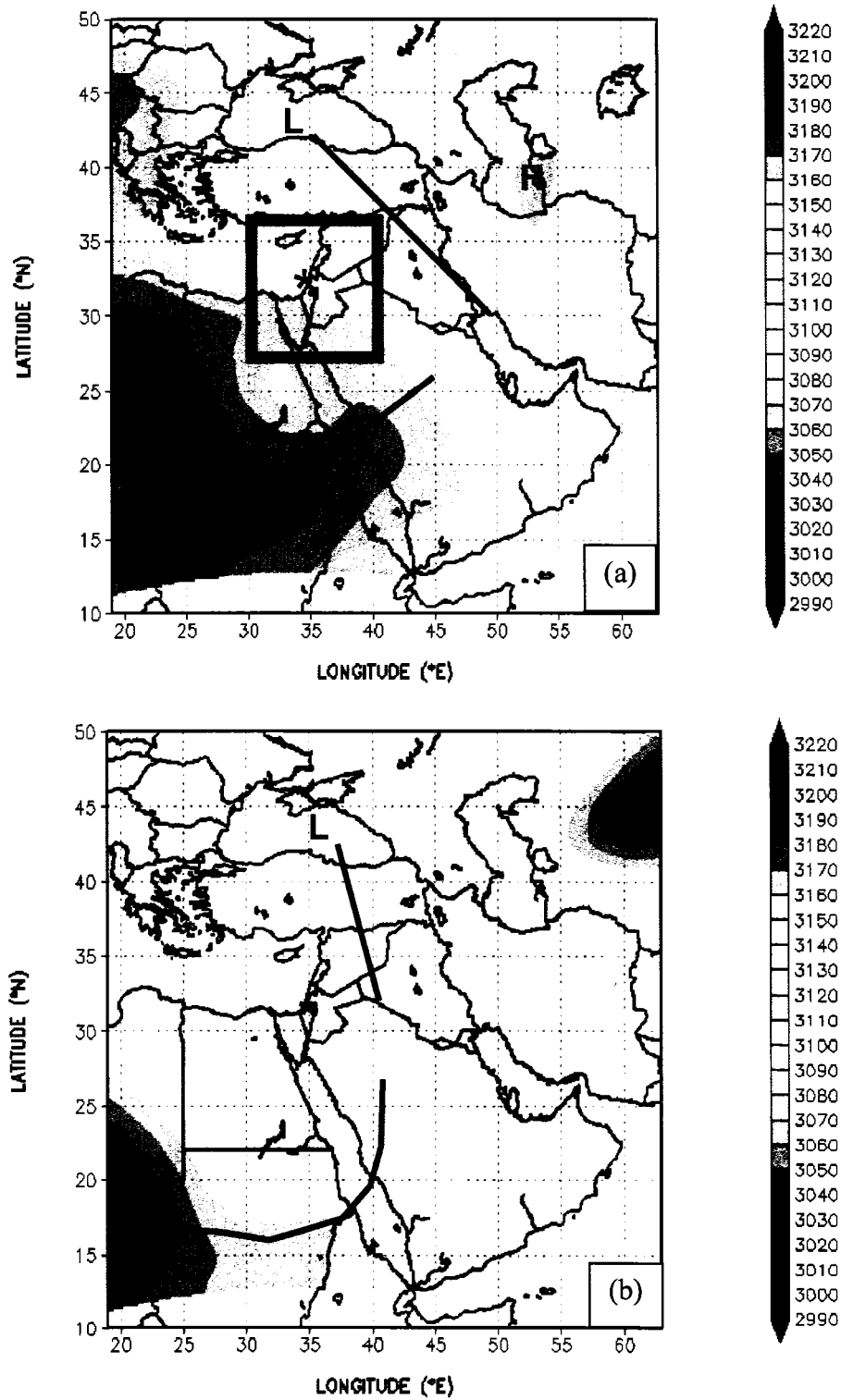
Fig. 6. 1997 ECMWF 700 hPa heights (m) at 0000 UTC (where asterisk marks study-
area center and box outlines MM5 Domain-1) on: (a) 29 July and (b) 31 July
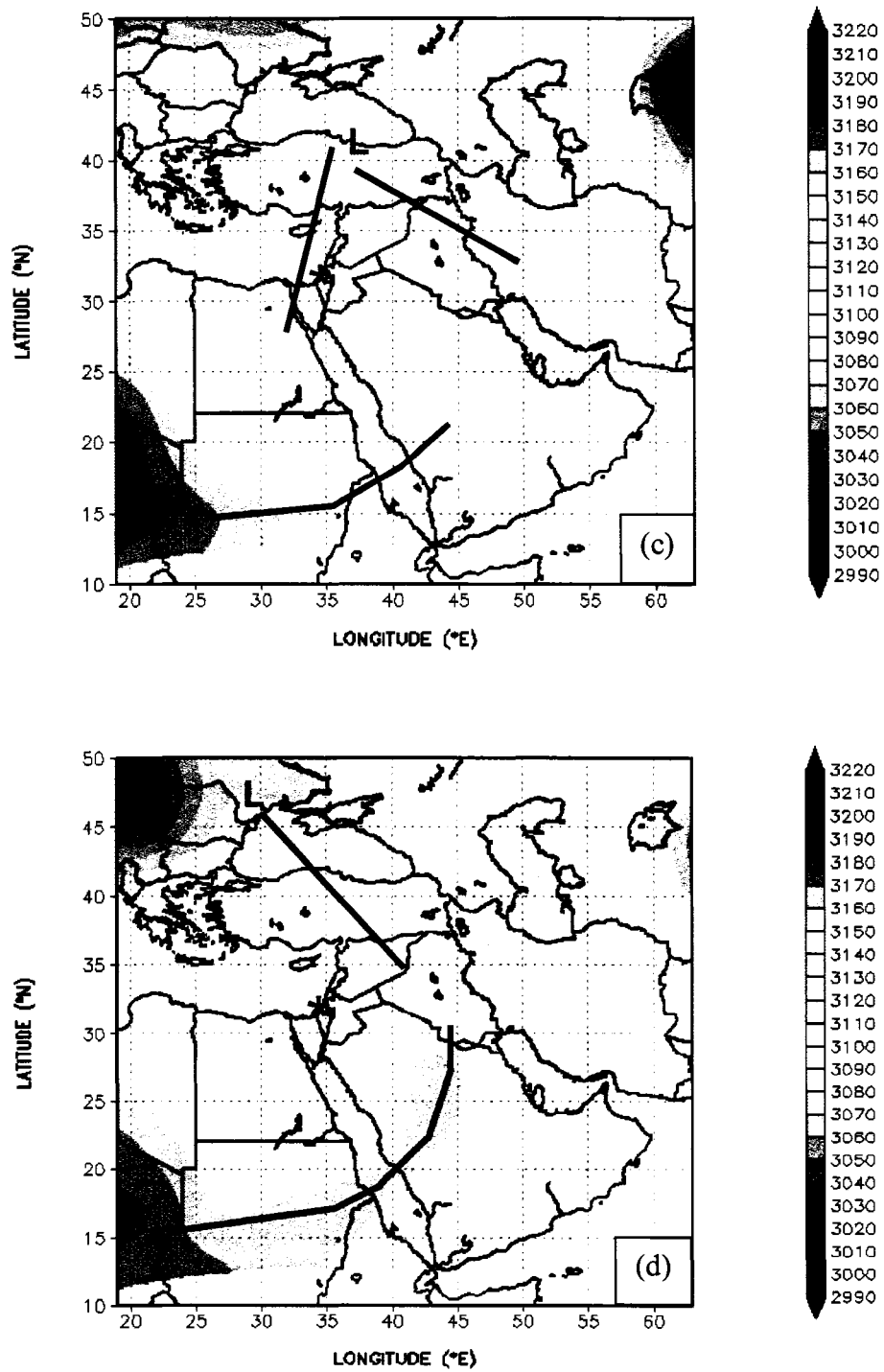
Fig. 6. 1997 ECMWF 700 hPa heights (m) at 0000 UTC (where asterisk marks study-area center) on: (c) 1 August and (d) 2 August
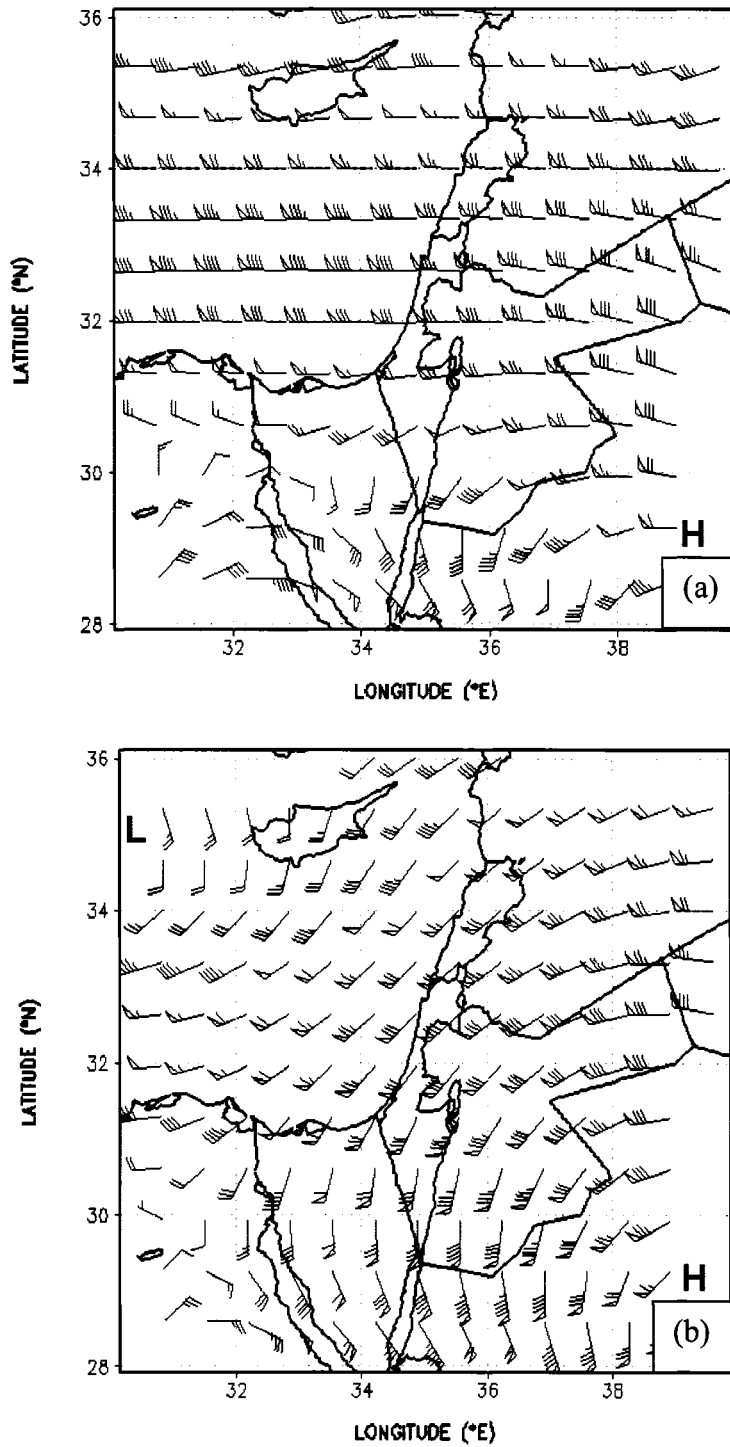
Fig. 7. 1997 ECMWF 700 hPa winds (flag is 5 m s^{-1} and barb is 1 m s^{-1}) in area of

MM5 Domain-1 at 0000 UTC on: (a) 29 July and (b) 31 July
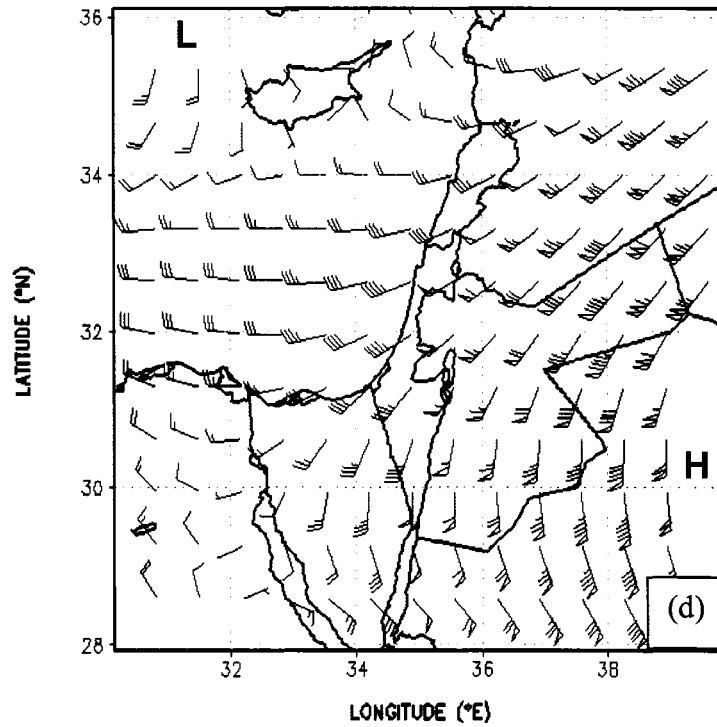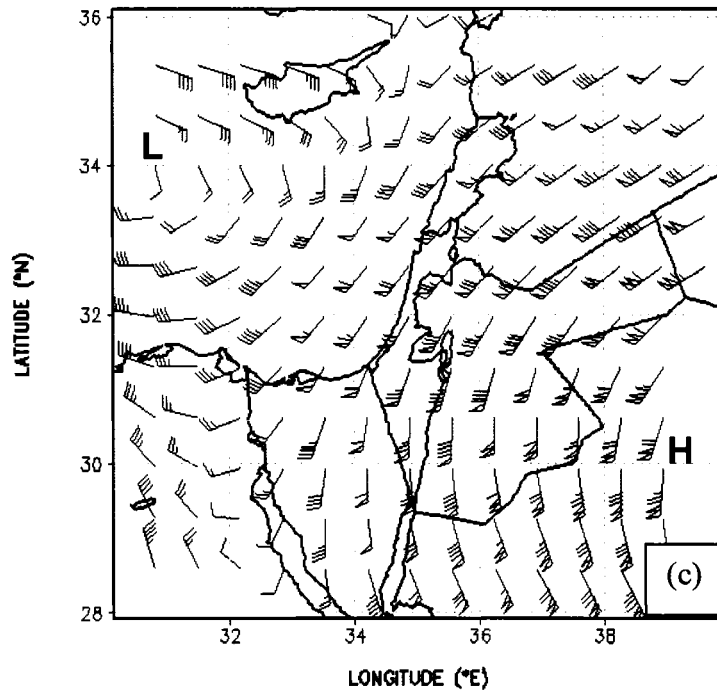
Fig. 7. 1997 ECMWF 700 hPa winds (flag is 5 m s^{-1} and barb is 1 m s^{-1}) in area of

MM5 Domain-1 at 0000 UTC on: (c) 1 August and (d) 2 August
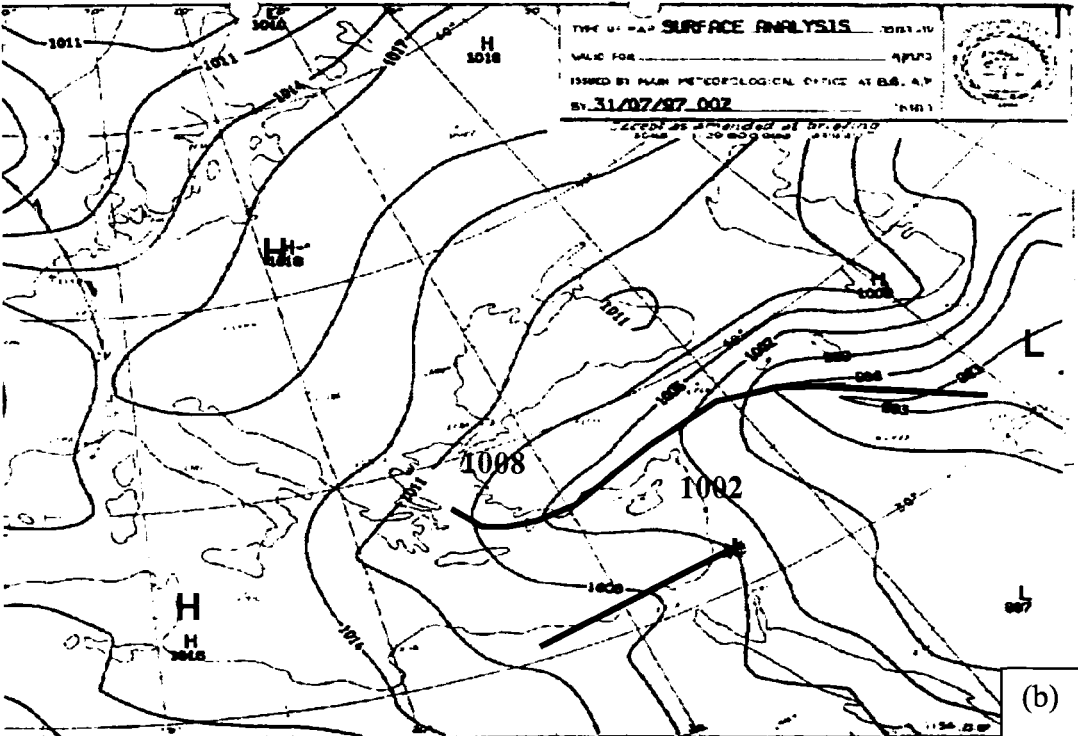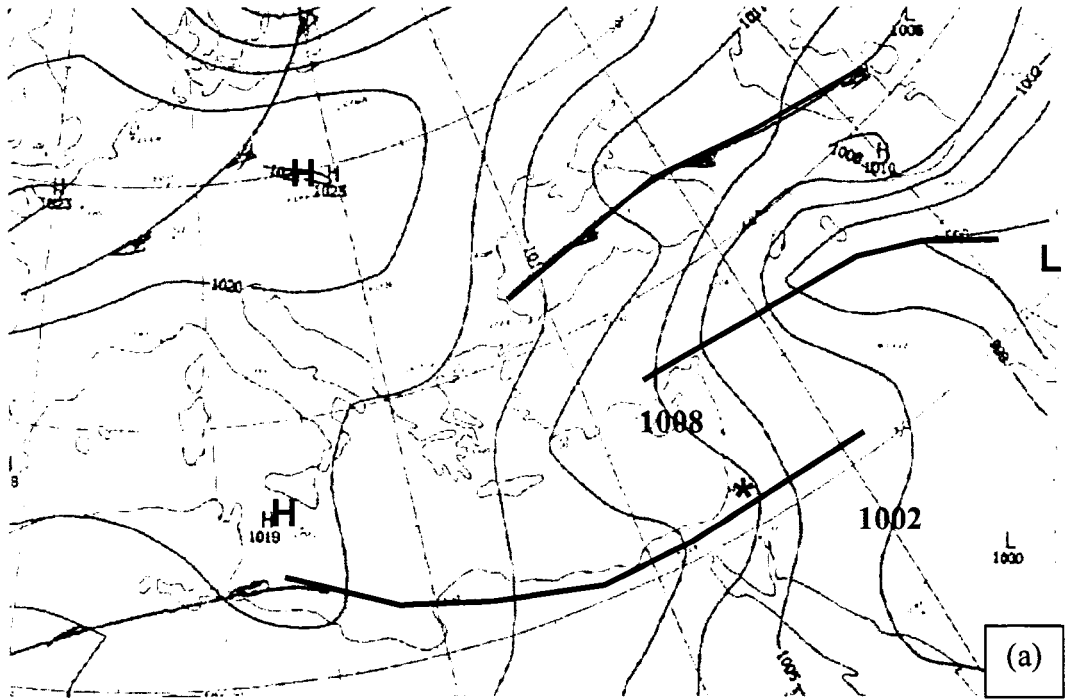
Fig. 8. 1997 IMS surface pressure (hPa) at 0000 UTC on: (a) 29 July and (b) 31 July

53
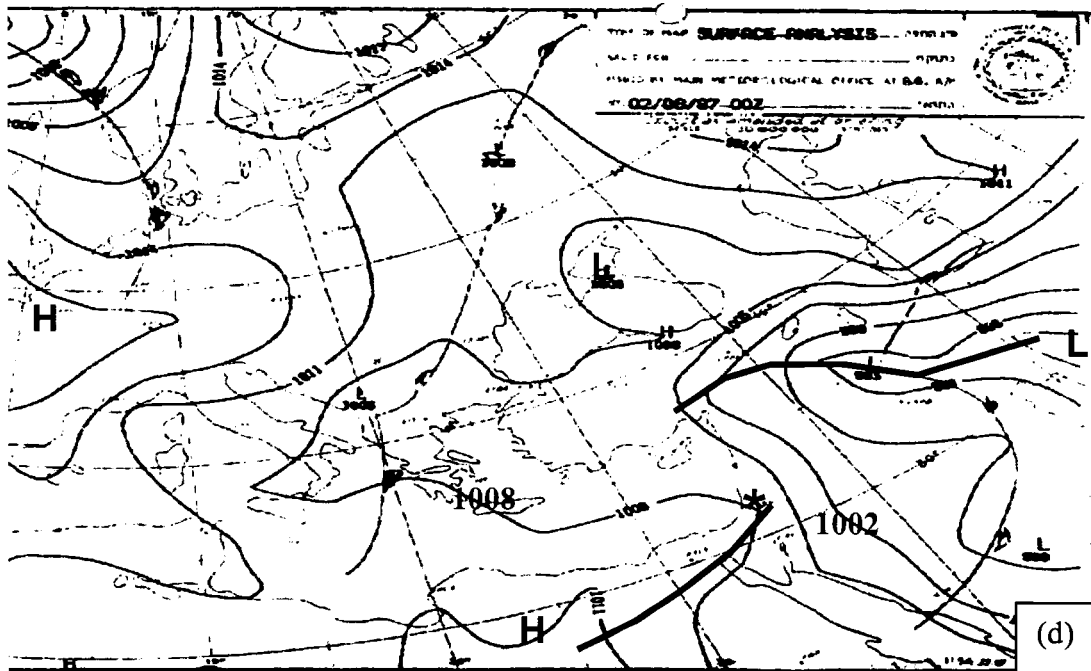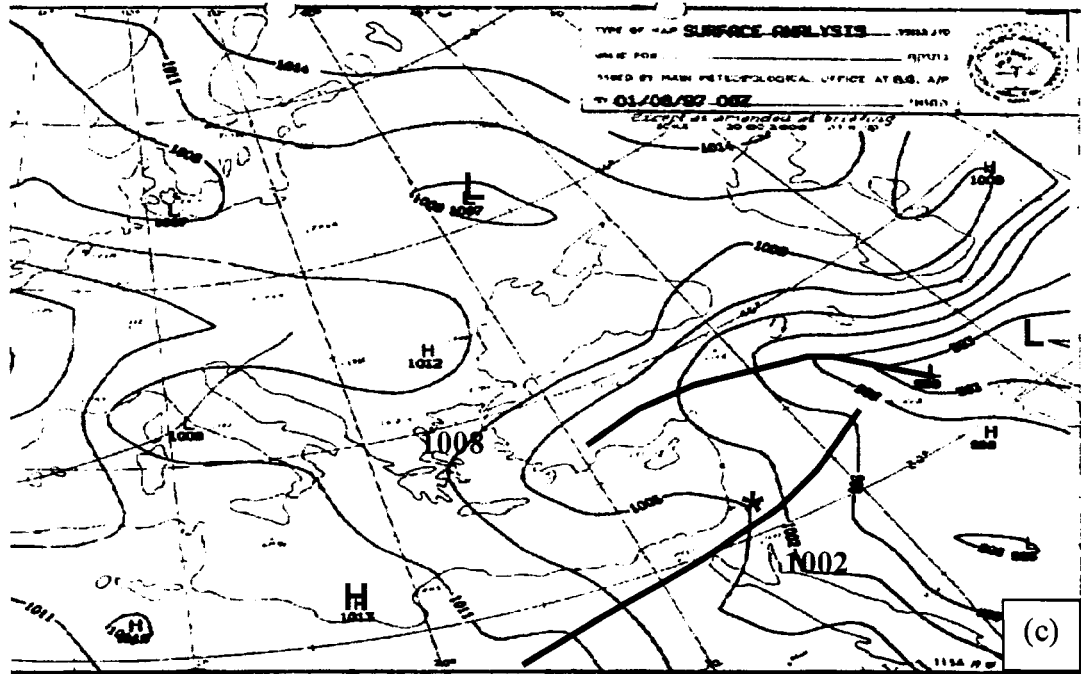
Fig. 8. 1997 IMS surface pressure (hPa) at 0000 UTC on: (c) 1 August and (d) 2 August
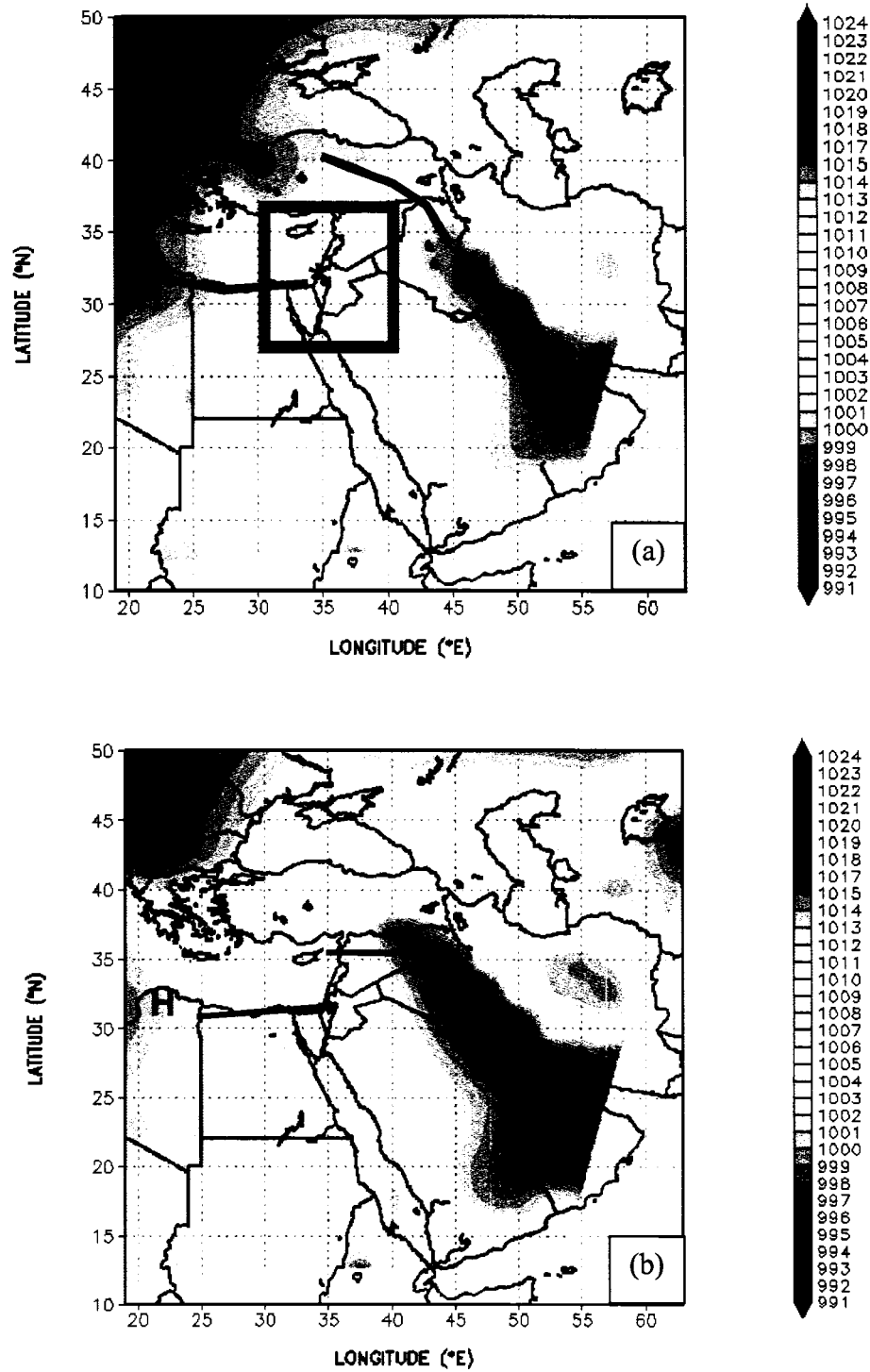
Fig. 9. 1997 ECMWF surface pressure (hPa) at 0000 UTC (where box is MM5

Domain-1) on: (a) 29 July and (b) 31 July
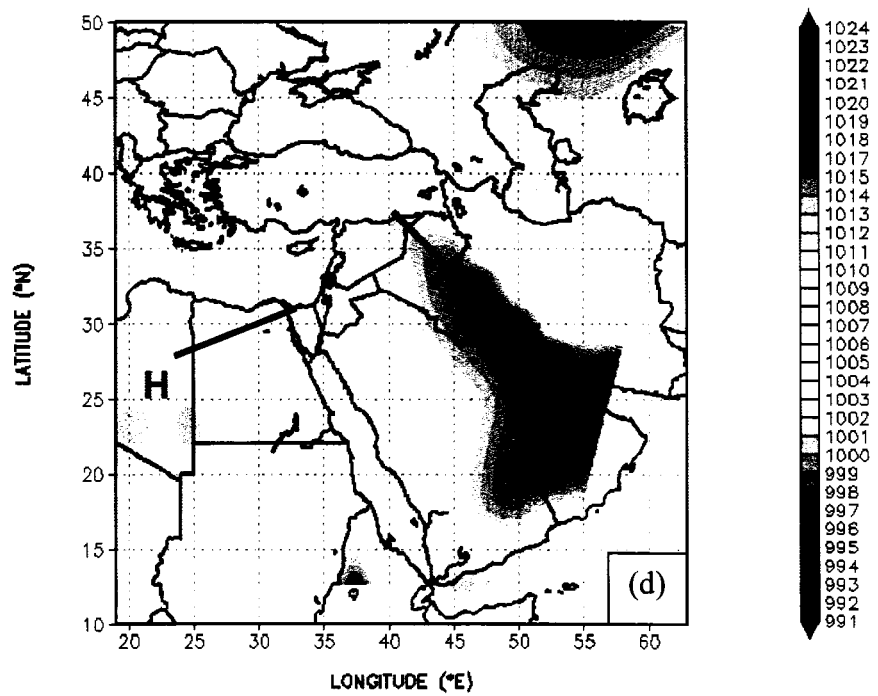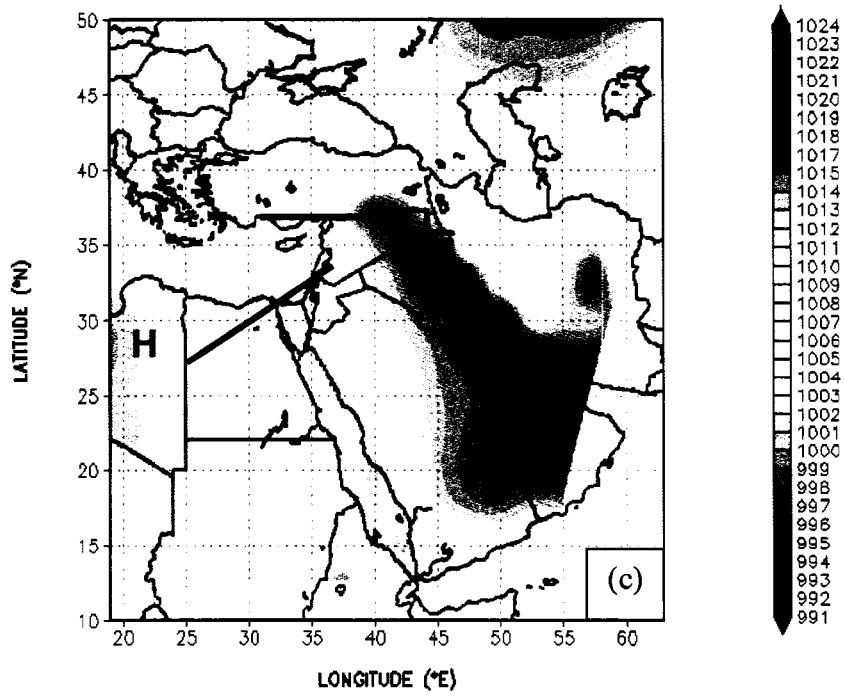
Fig. 9. 1997 ECMWF surface pressure (hPa) at 0000 UTC on: (c) 1 August and (d) 2
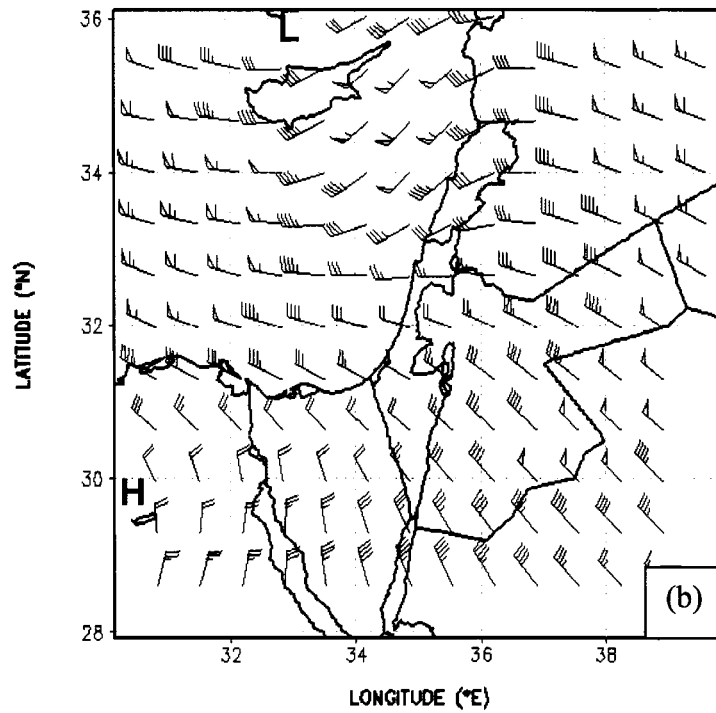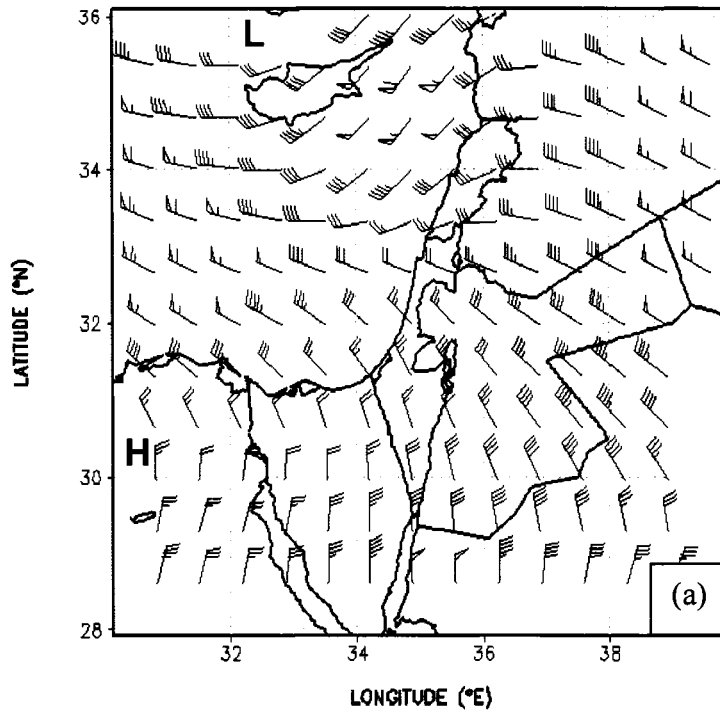
August

Fig. 10. 1997 ECMWF surface winds (where flag is 5 m s^{-1} and barb is 1 m s^{-1}) in

area of MM5 Domain-1 at 0000 UTC on: (a) 29 July and (b) 31 July
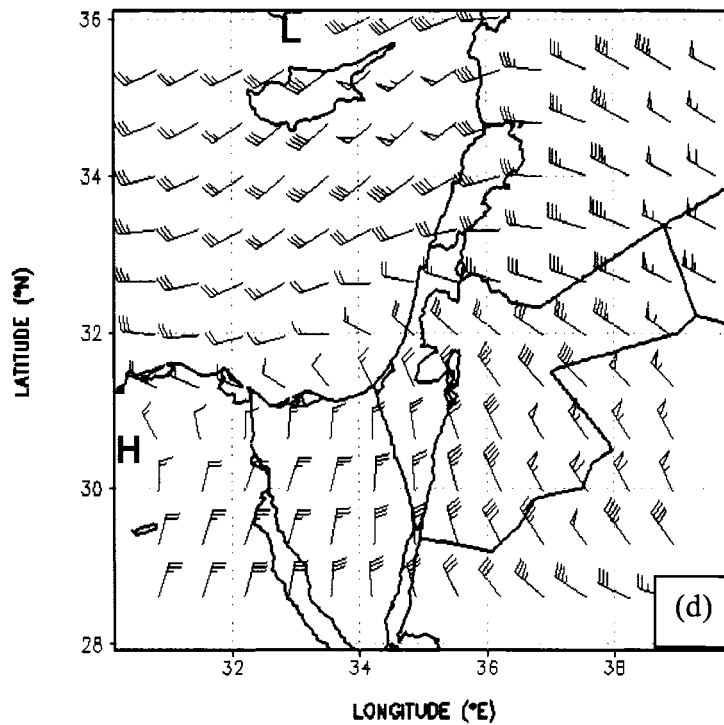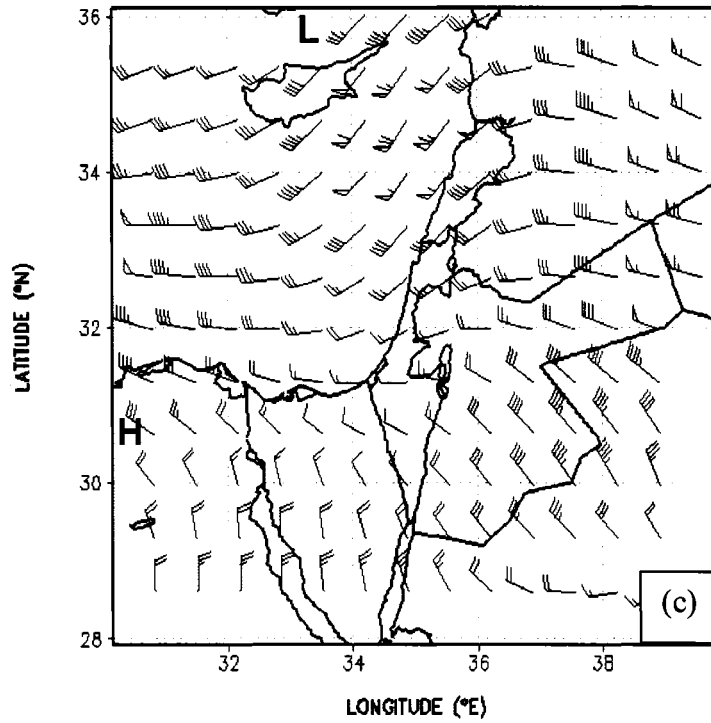
Fig. 10. 1997 ECMWF surface winds (where flag is 5 m s^{-1} and barb is 1 m s^{-1}) in

area of MM5 Domain-1 at 0000 UTC on: (c) 1 August and (d) 2 August
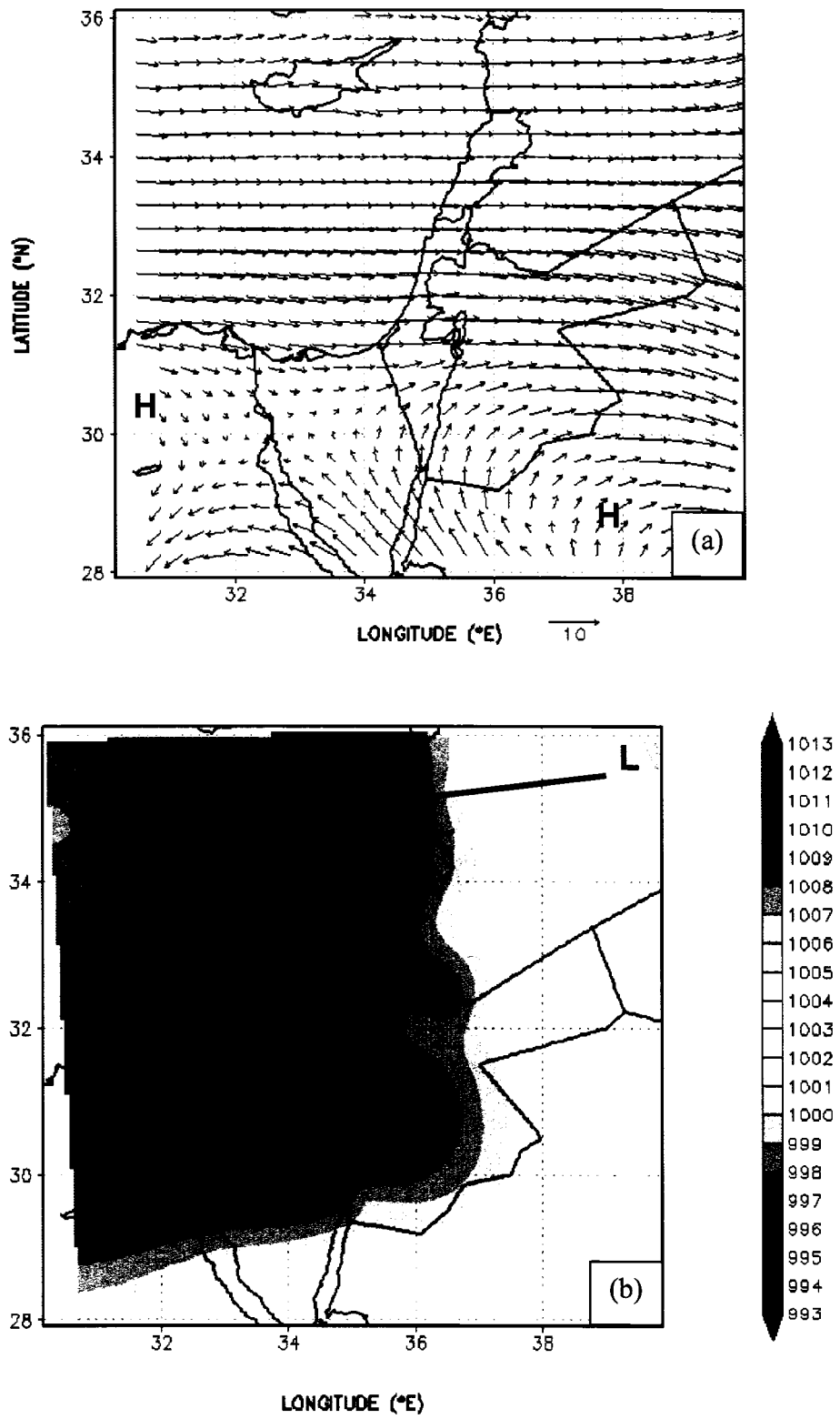
Fig. 11. MM5 0000 UTC 29 July 1997 Domain-1: (a) 700 hPa wind and (b) surface
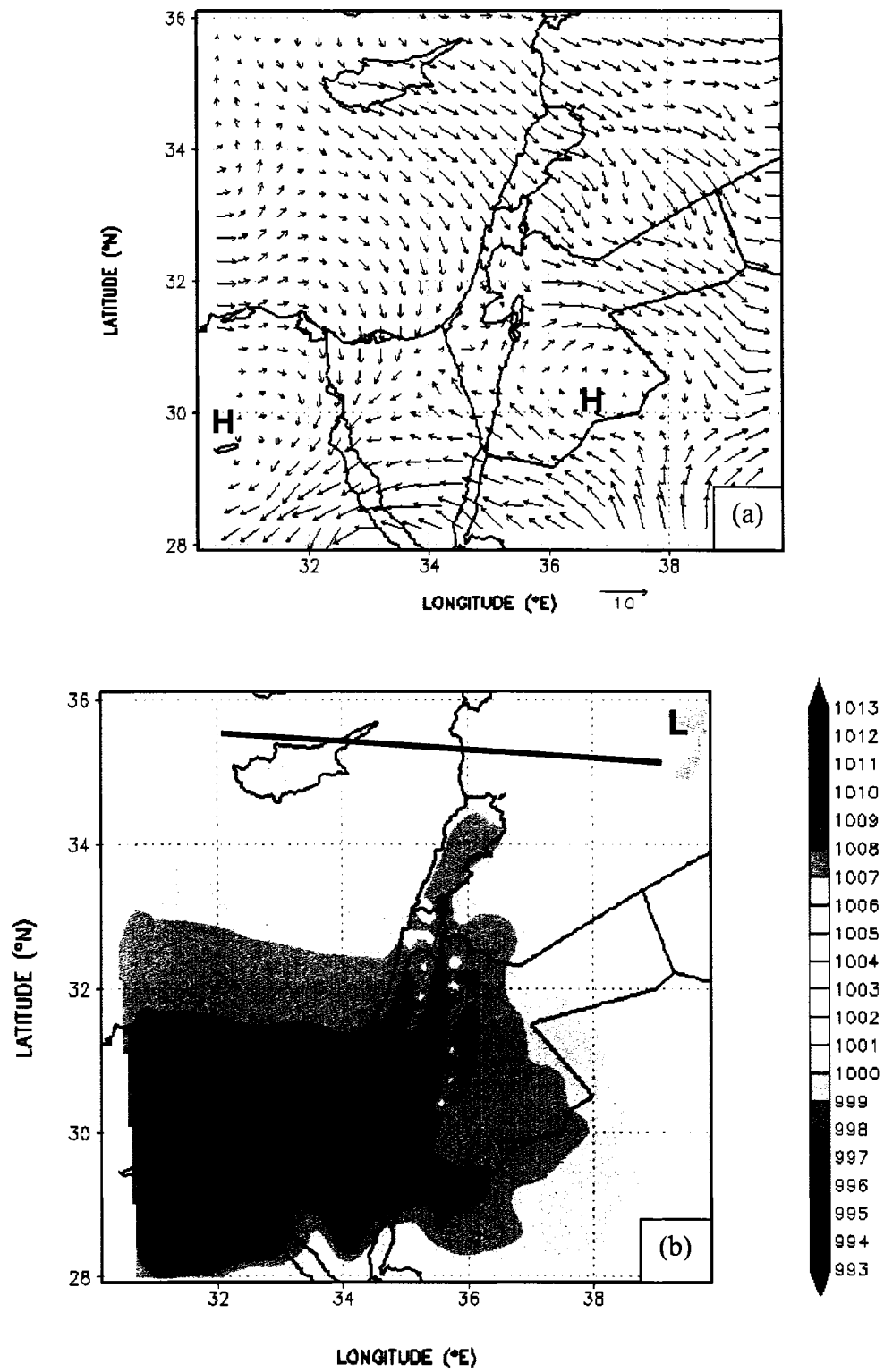
pressure

Fig. 12. MM5 0000 UTC 31 July 1997 Domain-1: (a) 700 hPa wind and (b) surface
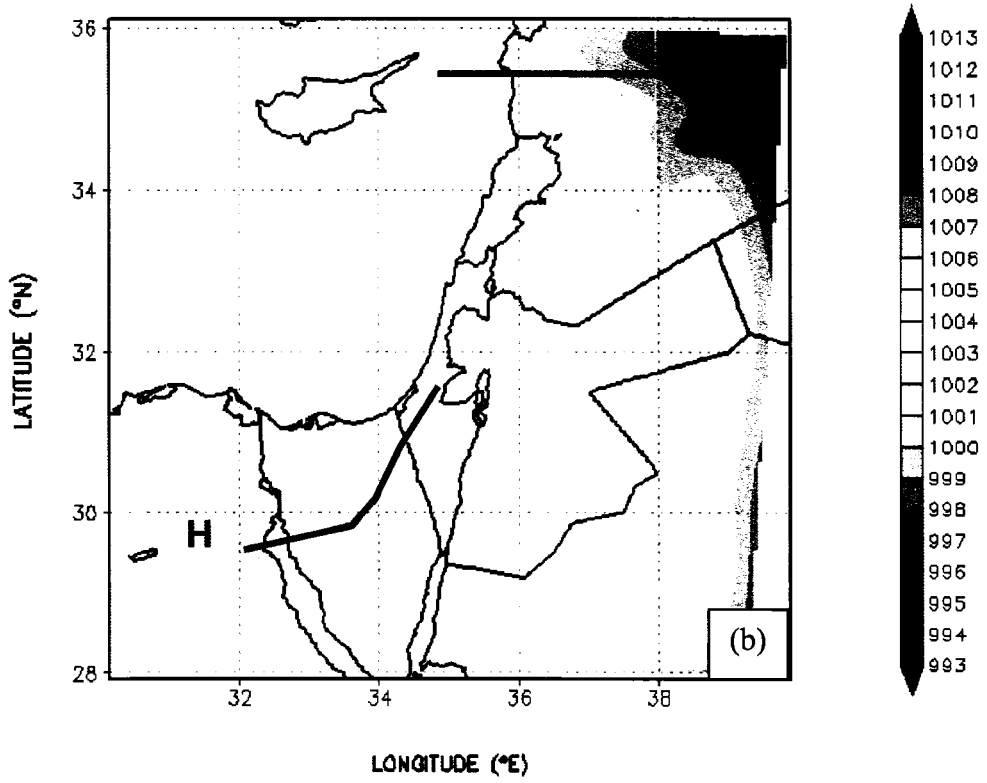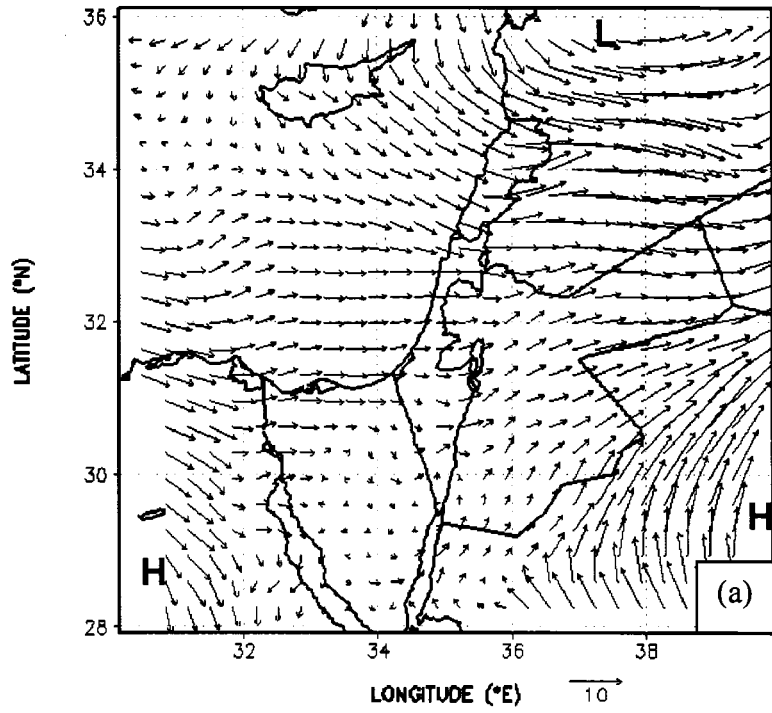
pressure

Fig. 13. . MM5 0000 UTC 1 August 1997 Domain-1: (a) 700 hPa wind and (b)
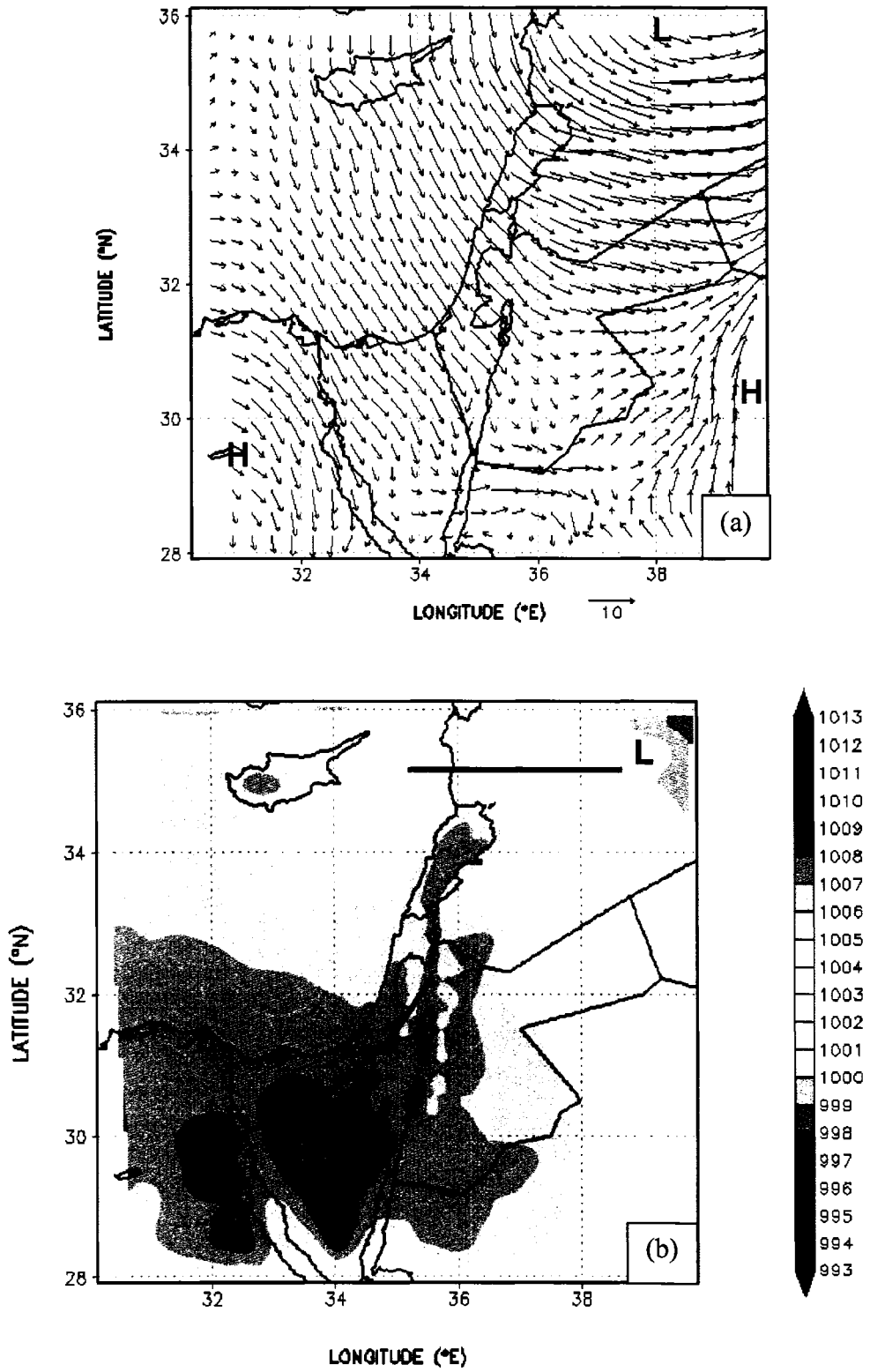
surface pressure

Fig. 14. MM5 0000 UTC 2 August 1997 Domain-1: (a) 700 hPa wind and (b) surface

pressure
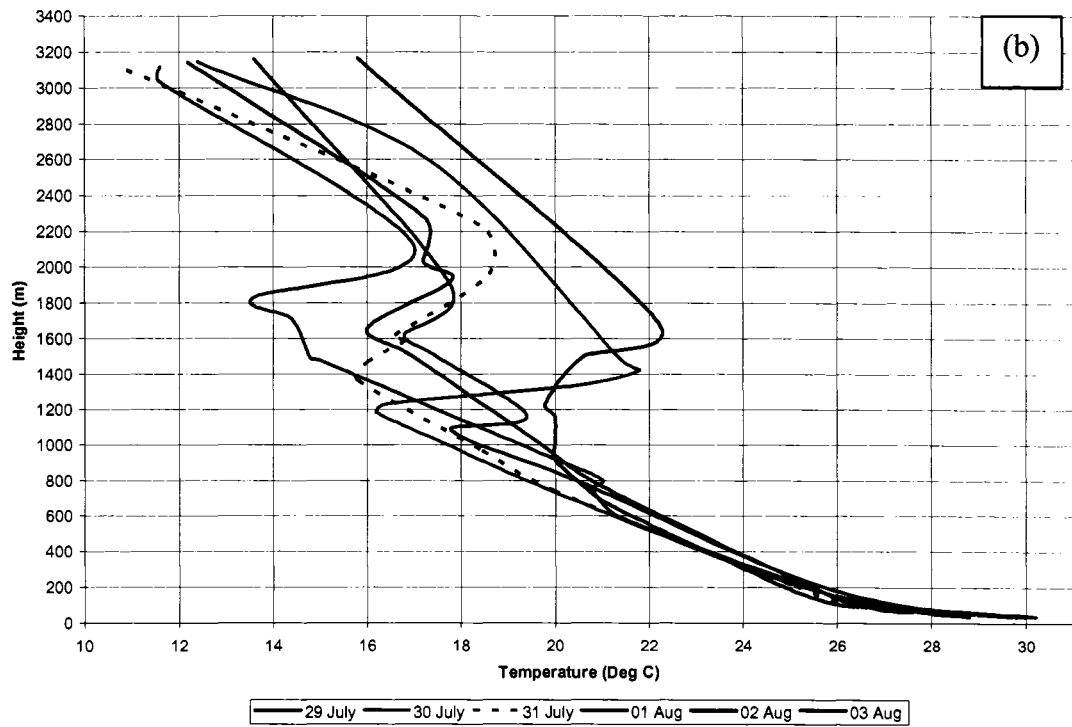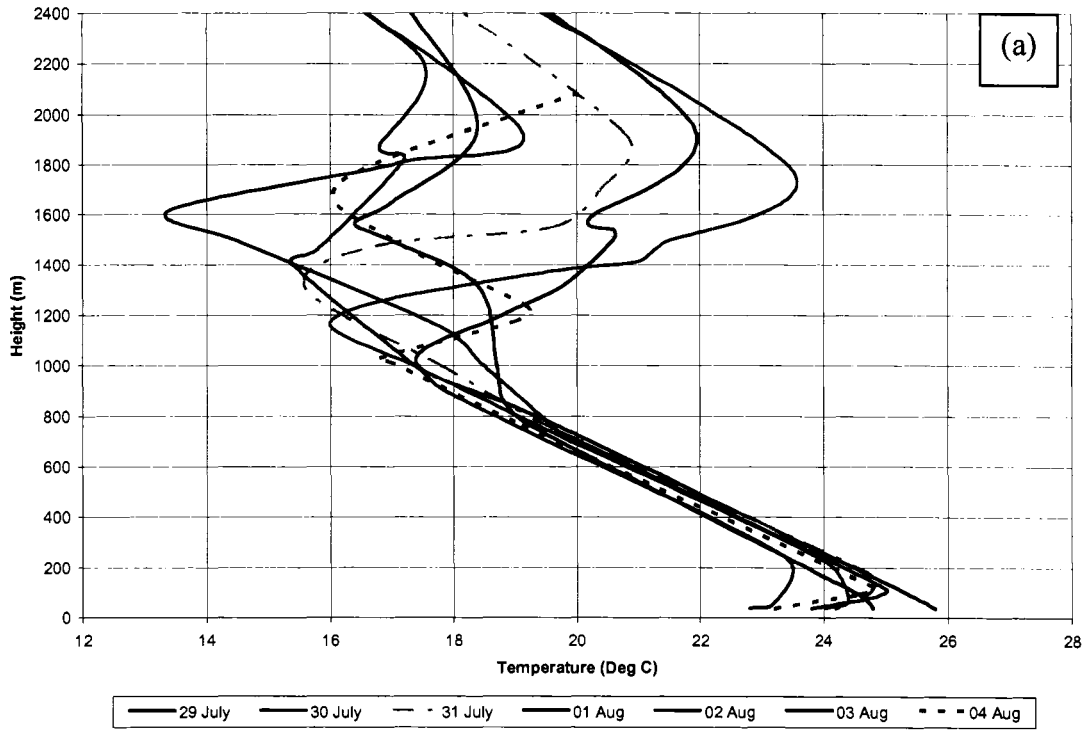
Fig. 15. 1997 Rawinsonde temperatures profiles for: (a) 1200 and (b) 0000 UTC
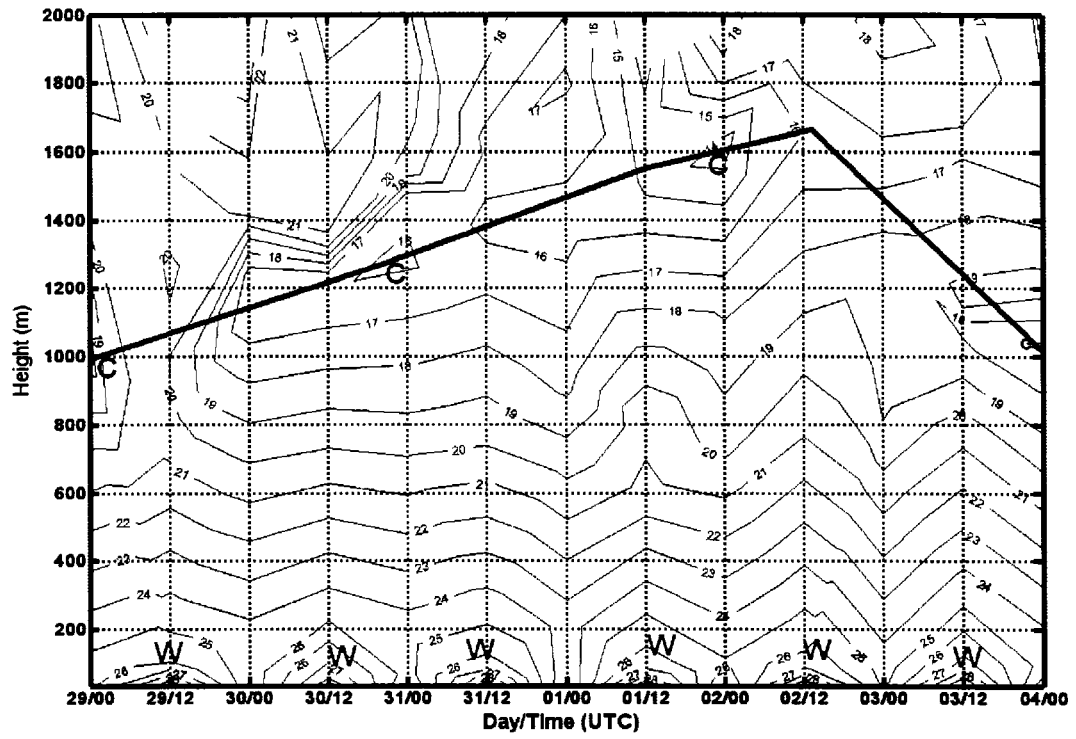
Fig. 16. Rawinsonde vertical time-height July-August 1997 temperature (^{0}C) cross

section, where solid line represents inversion base
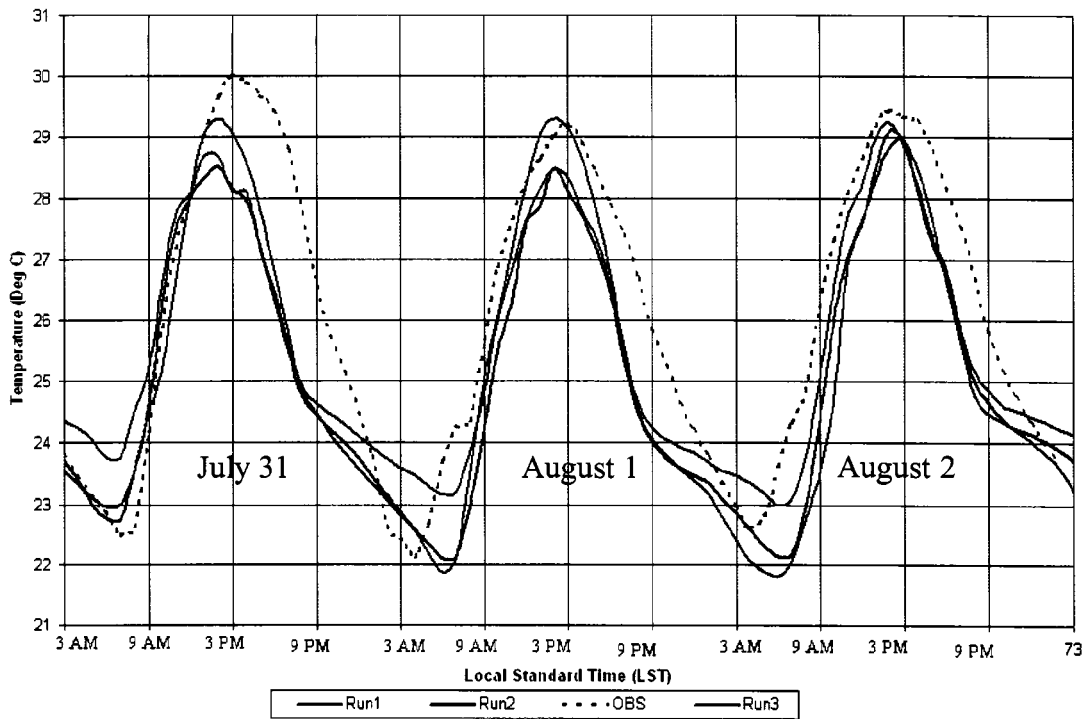
Fig. 17. 1997 observed and MM5 Domain-2 temperatures
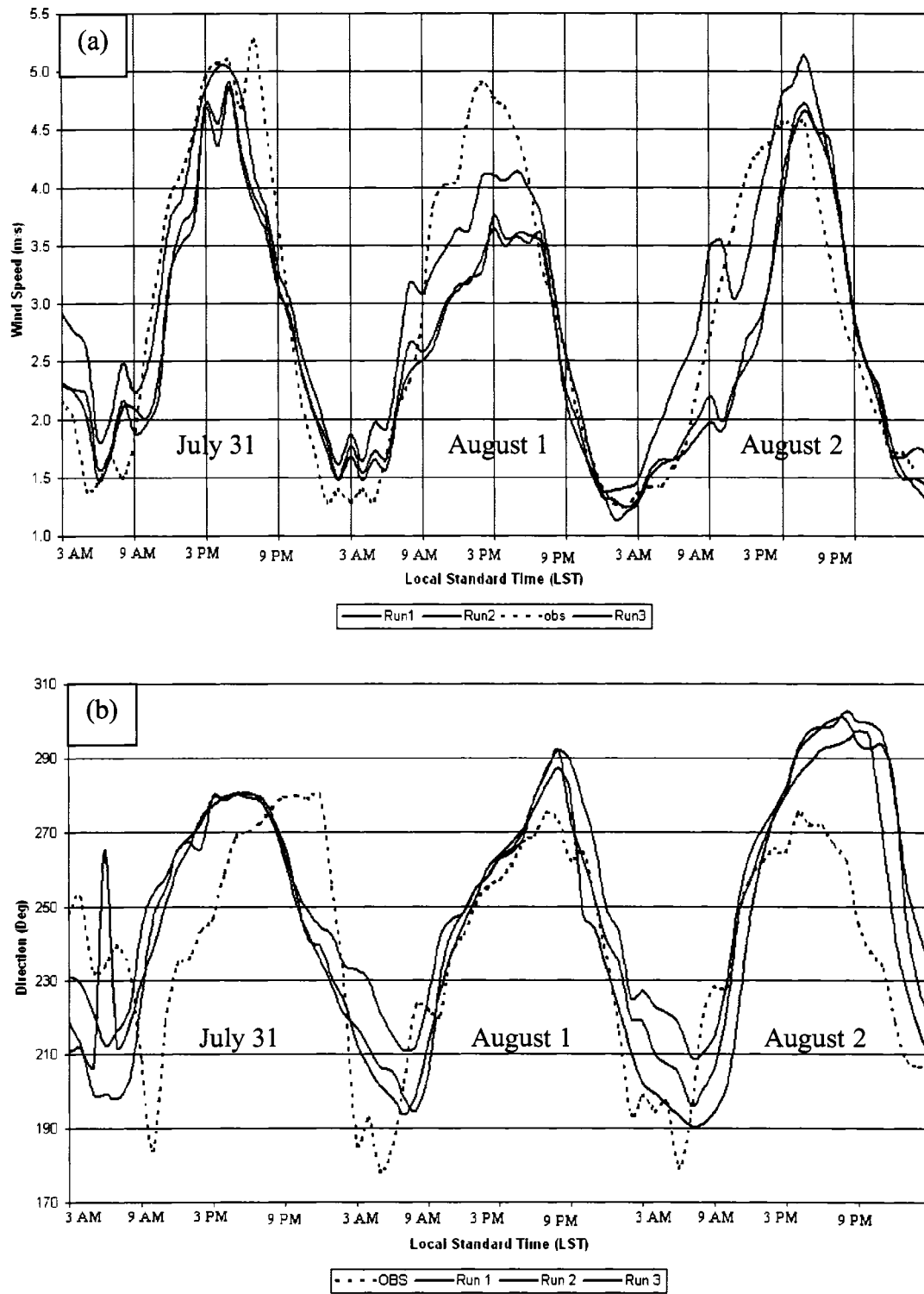
Fig. 18. 1997 observed and MM5 Domain-2 for: (a) wind speed and (b) wind

directions
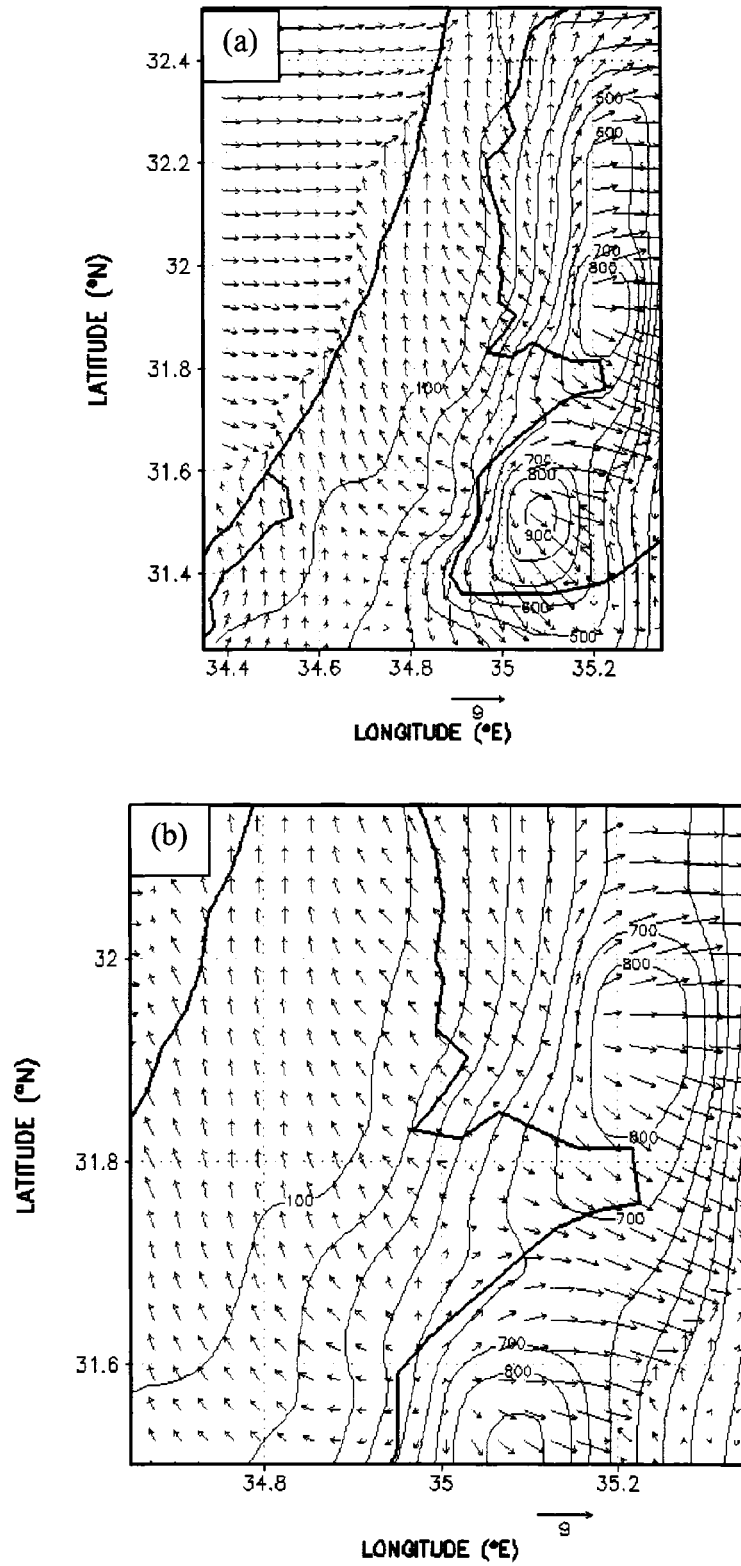
Fig. 19. MM5 Domain-3 winds at 0300 LST on 1 August 1997 for: (a) full and (b)
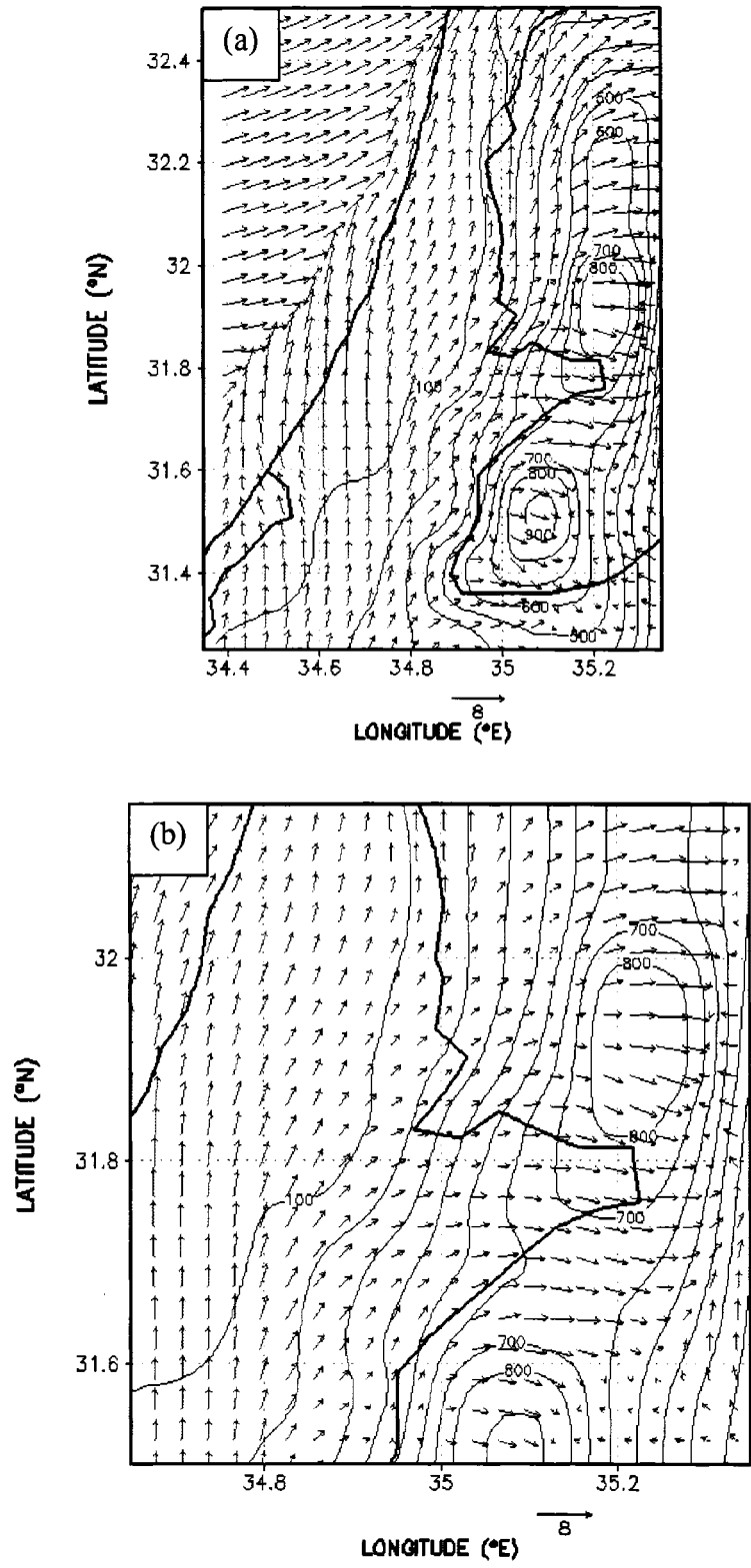
zoomed

Fig. 20. . MM5 Domain-3 winds at 0900 LST on 1 August 1997 for: (a) full and (b)
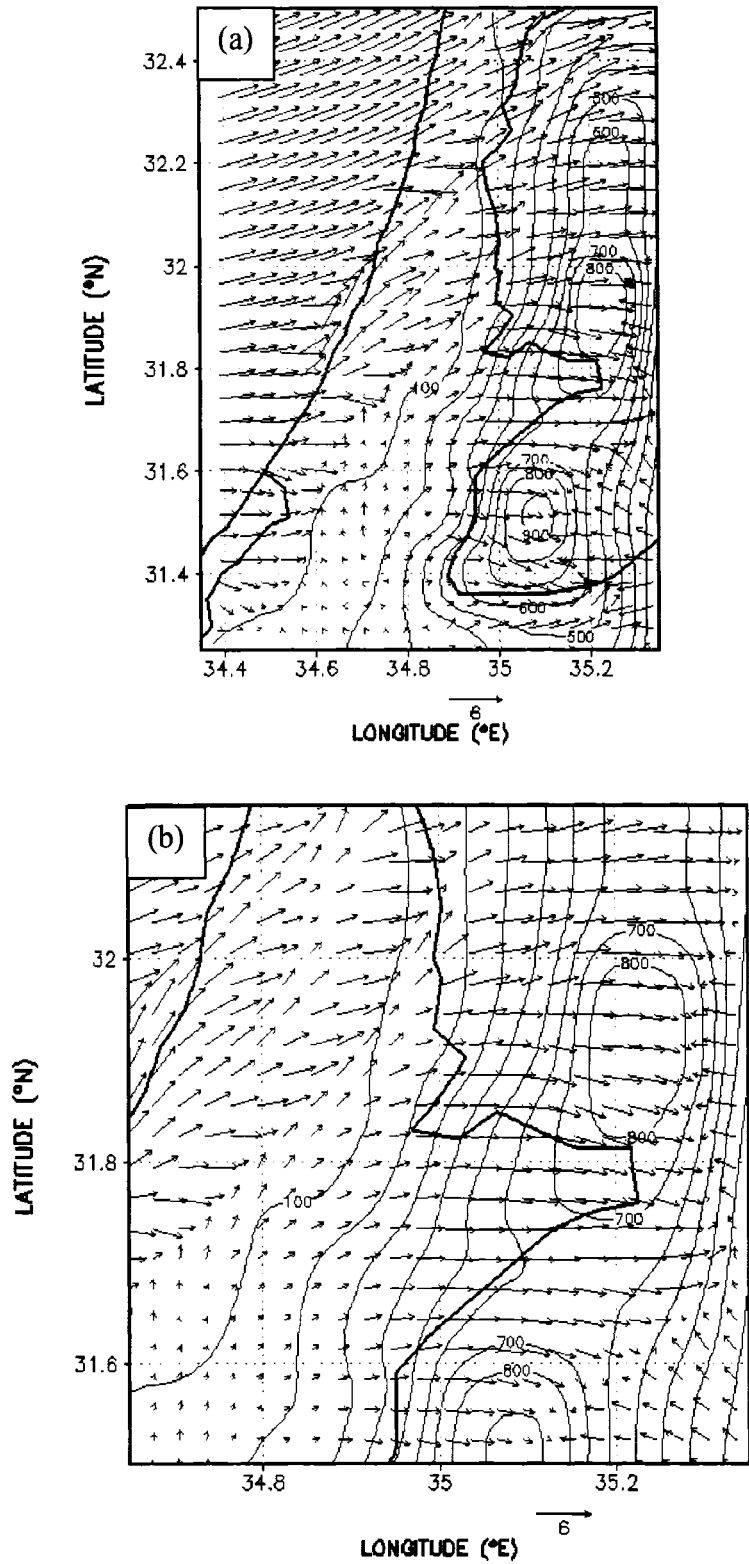
zoomed

Fig. 21. MM5 Domain-3 winds at 1100 LST on 1 August 1997 for: (a) full and (b)
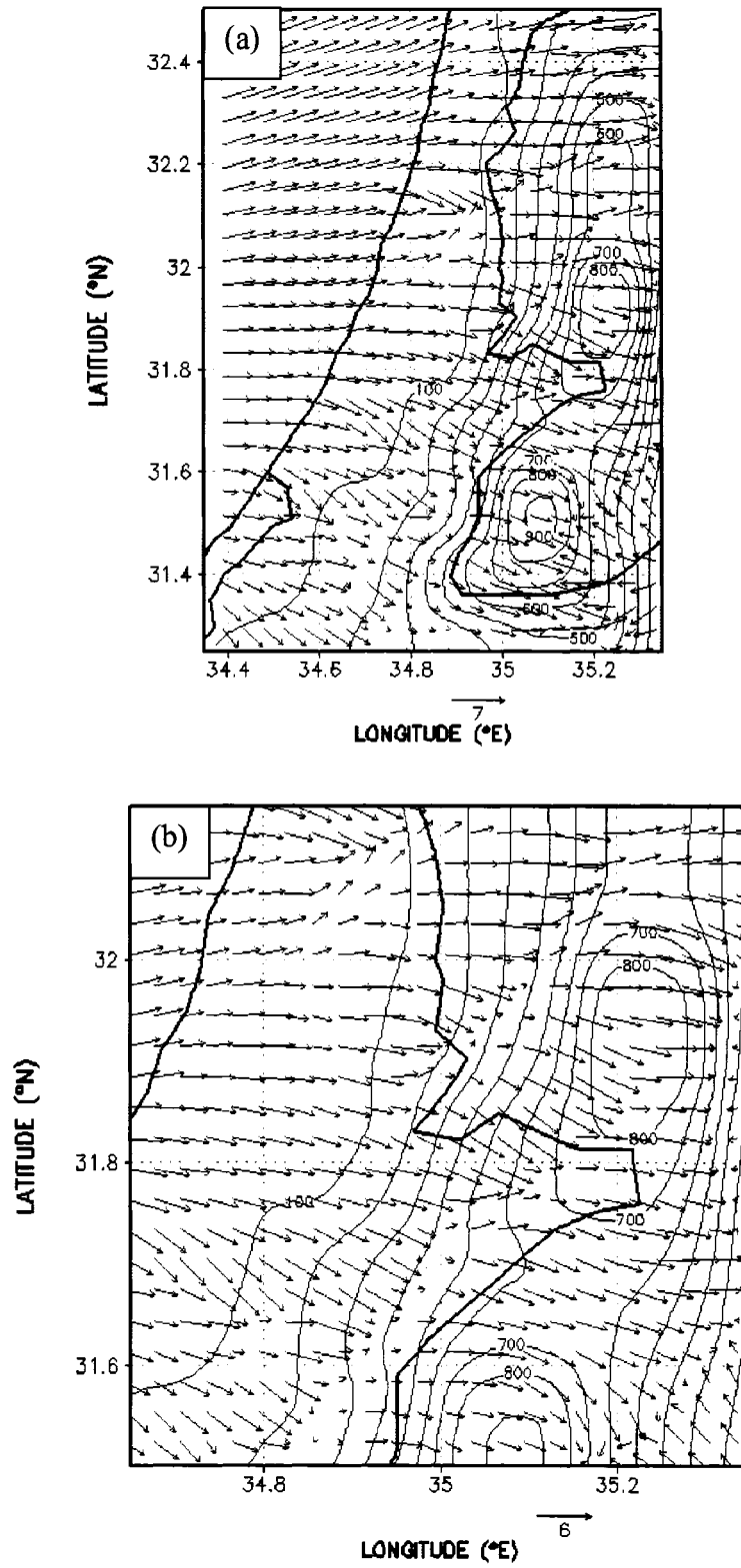
zoomed

Fig. 22. MM5 Domain-3 winds at 1300 LST on 1 August 1997 for: (a) full and (b)
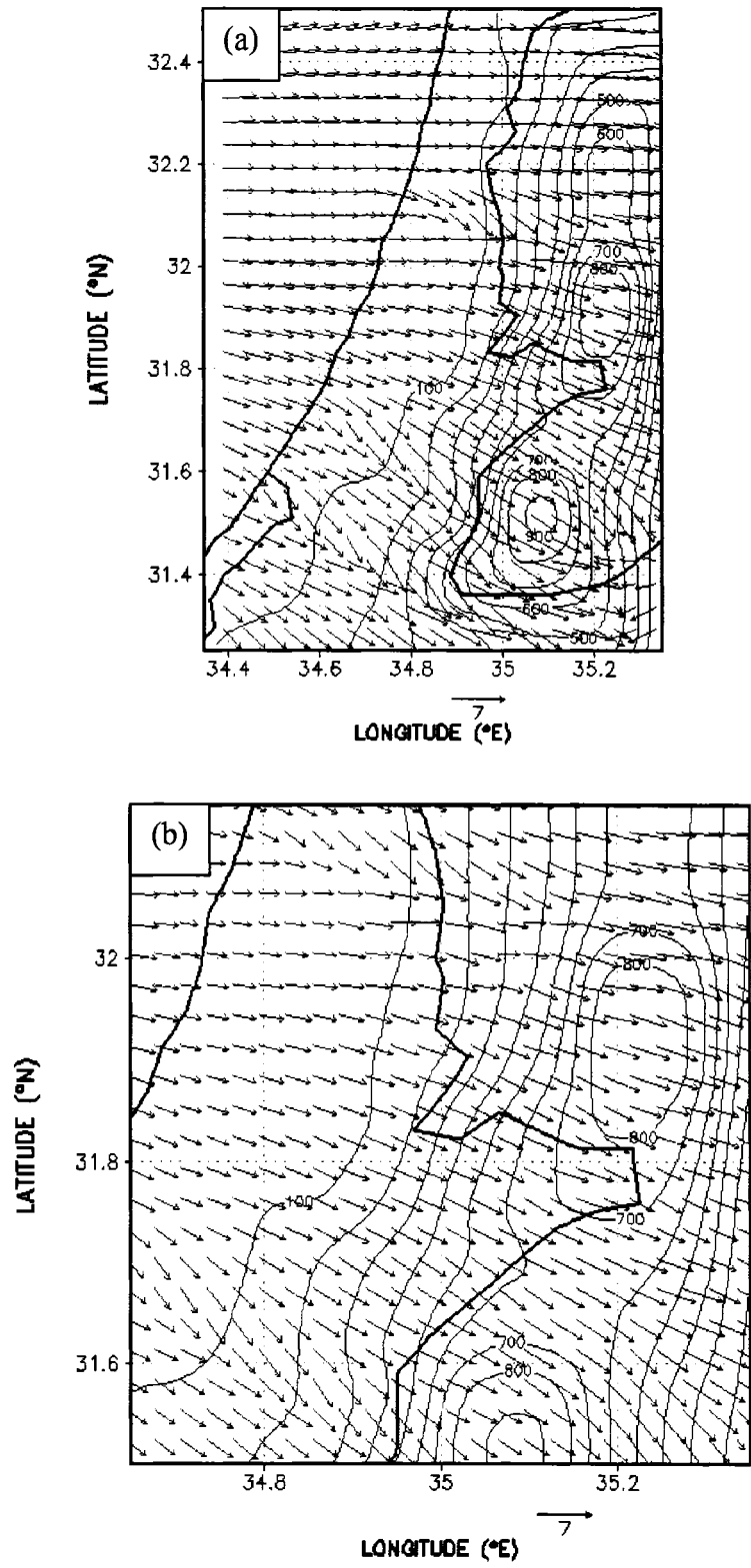
zoomed

Fig. 23. MM5 Domain-3 winds at 1600 LST on 1 August 1997 for: (a) full and (b)

zoomed

71
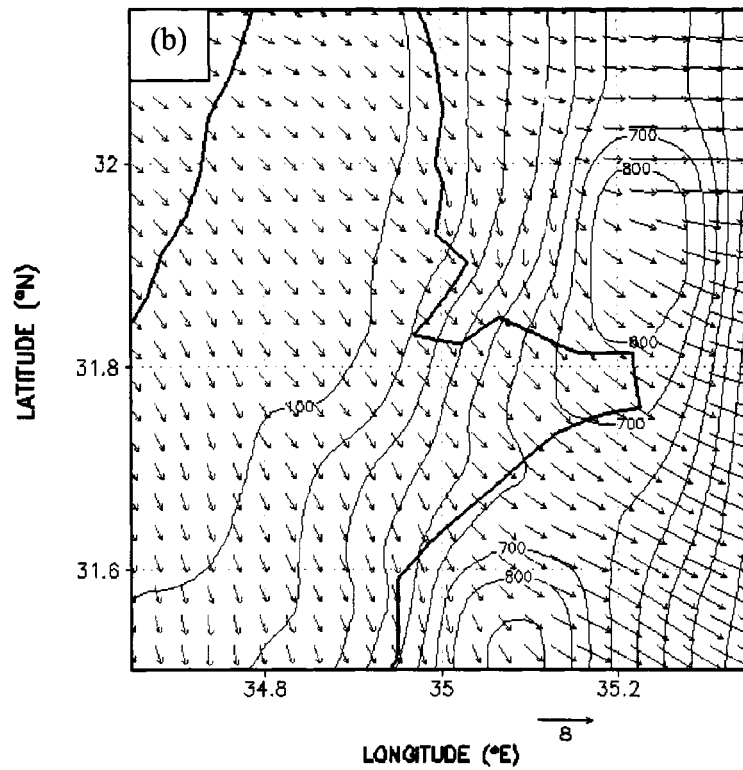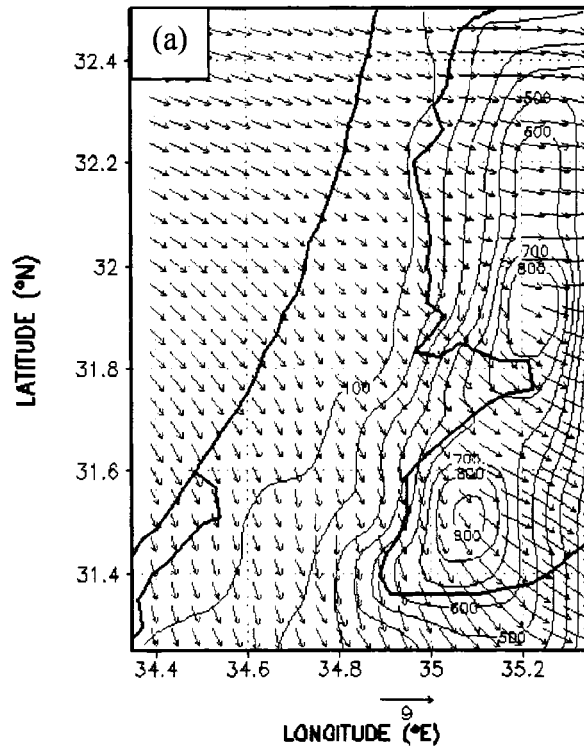
Fig. 24. MM5 Domain-3 winds at 2000 LST on 1 August 1997 for: (a) full and (b)
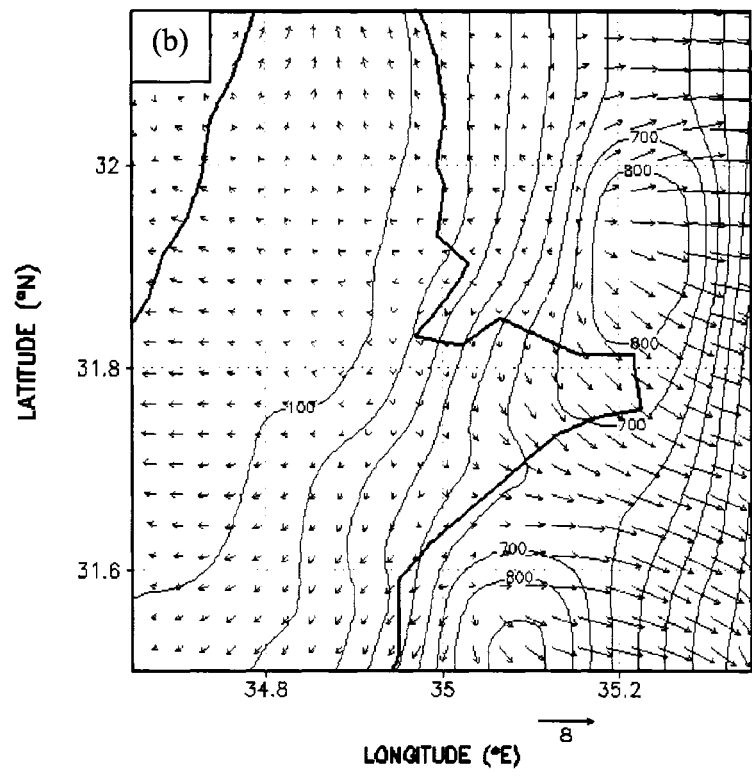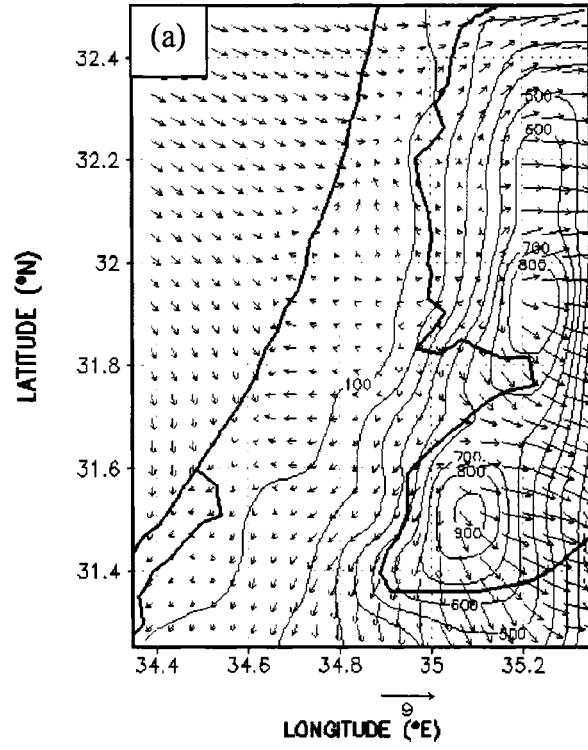
zoomed

Fig. 25. MM5 Domain-3 winds at 2300 LST on 1 August 1997 for: (a) full and (b)
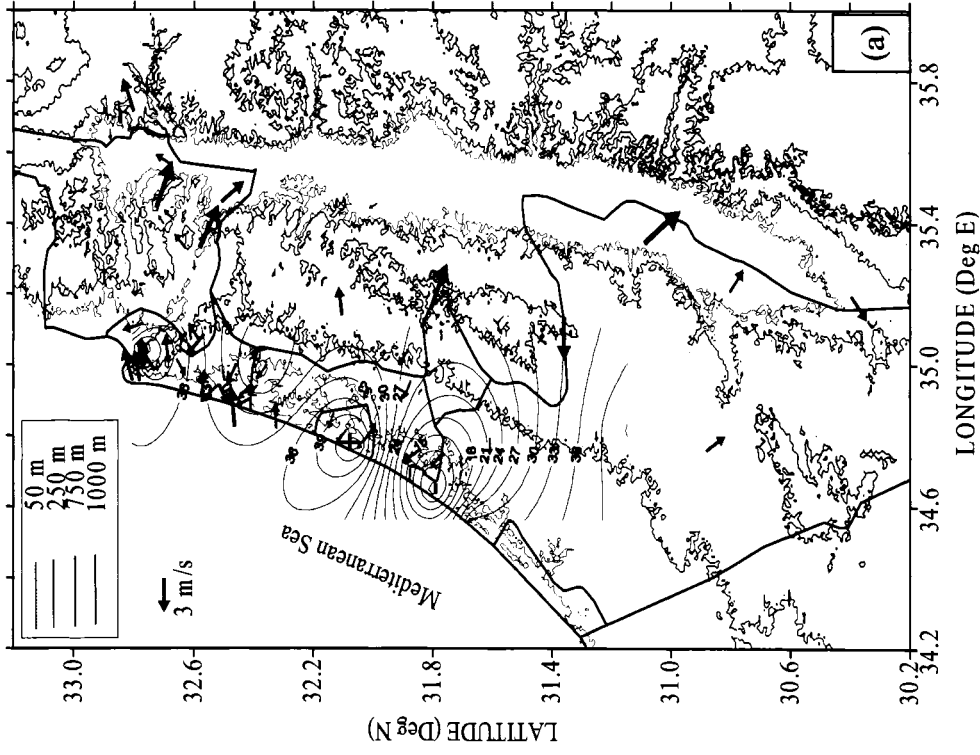
zoomed
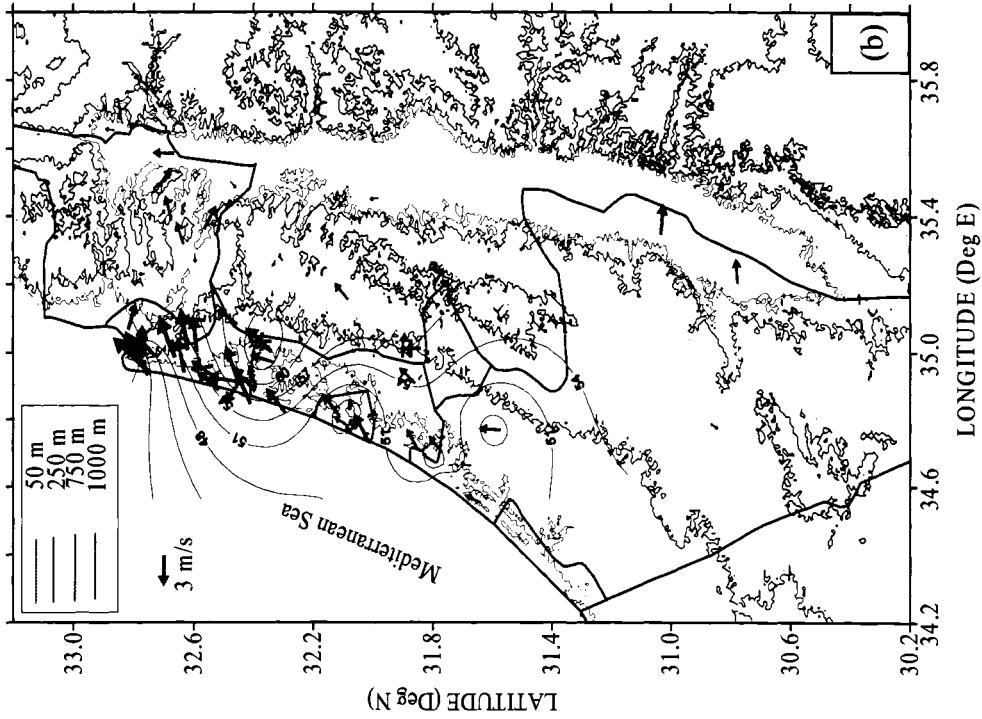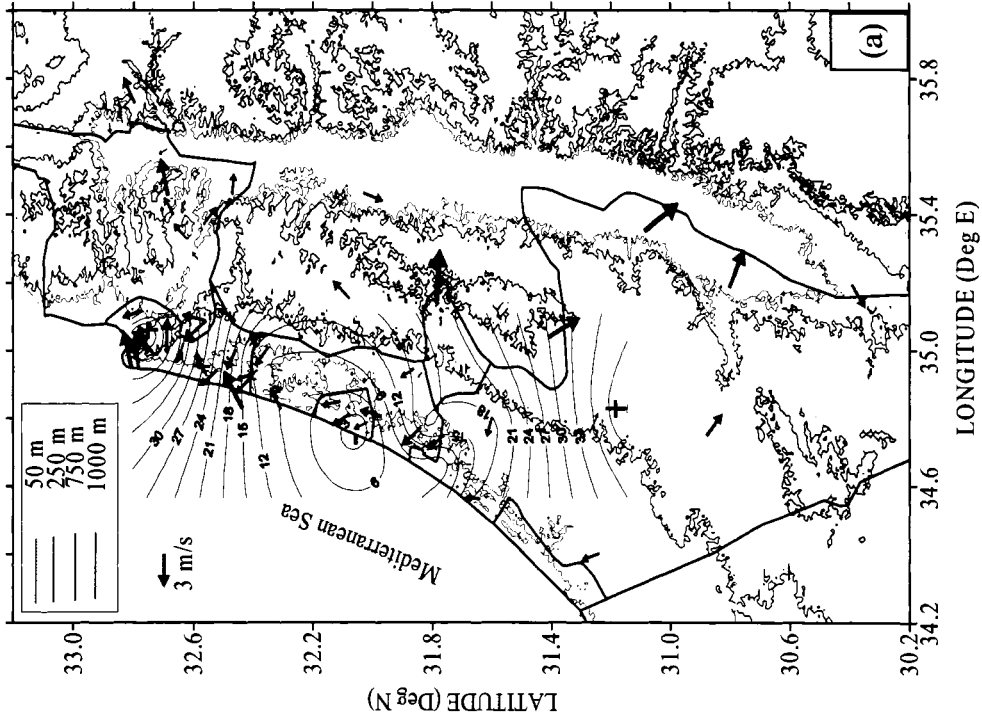
Fig. 26. Observed surface O$_3$ (ppb) and winds on 1 August 1997 at:
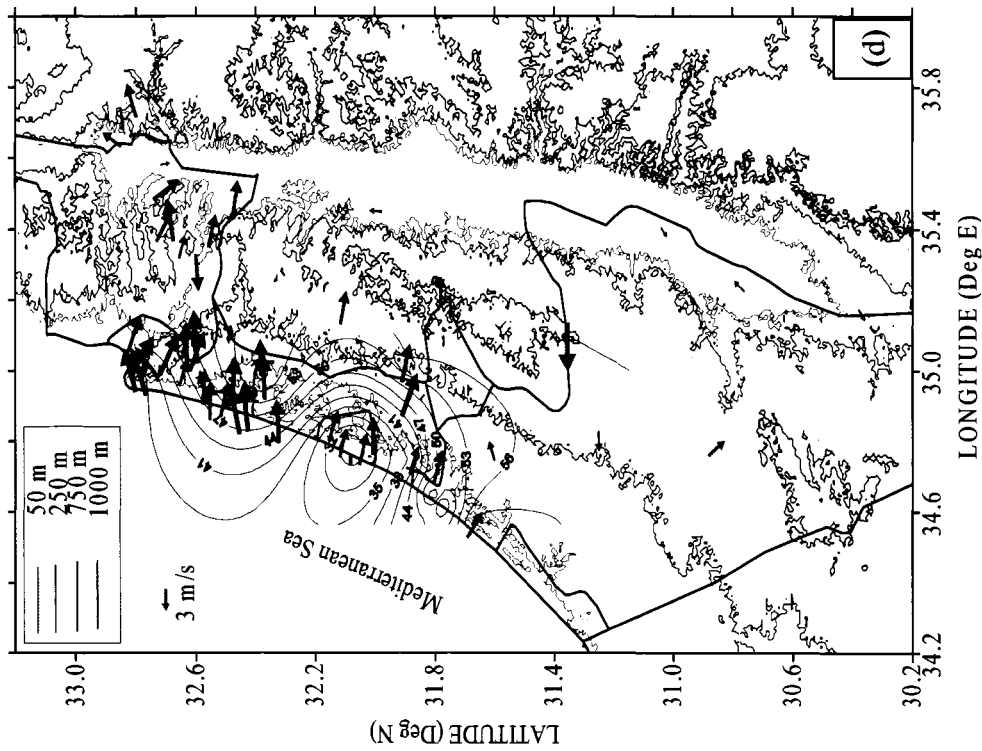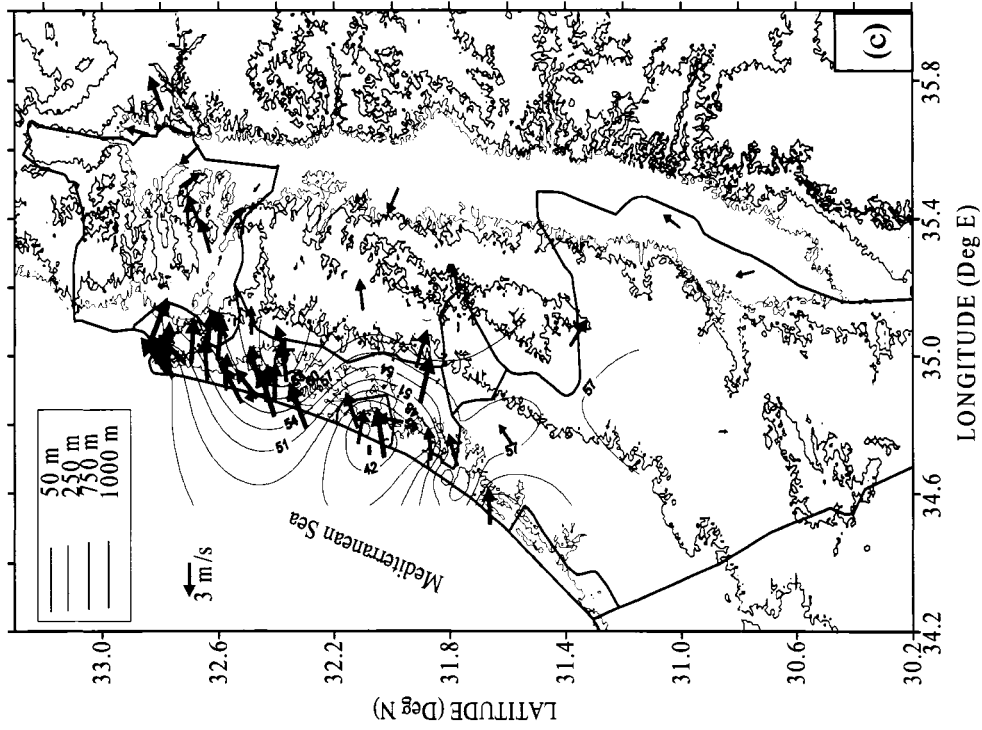
(a) 0300 and (b) 0900 LST

74
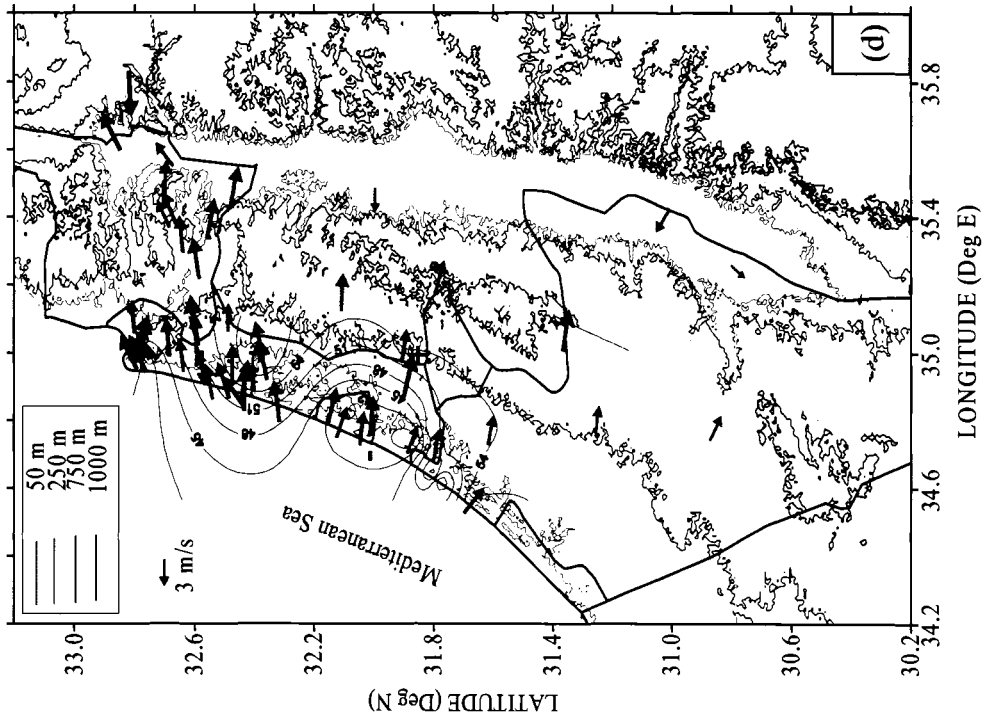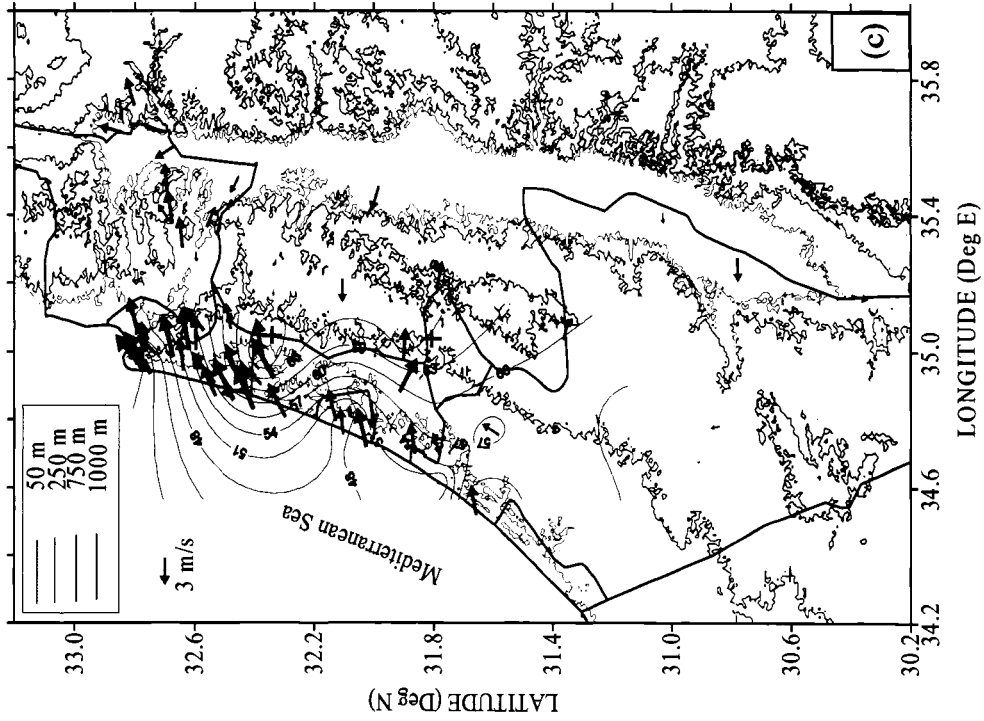
Fig. 26. Observed surface O$_3$ (ppb) and winds on 1 August 1997 at:
(c) 1100 and (d) 1600 LST
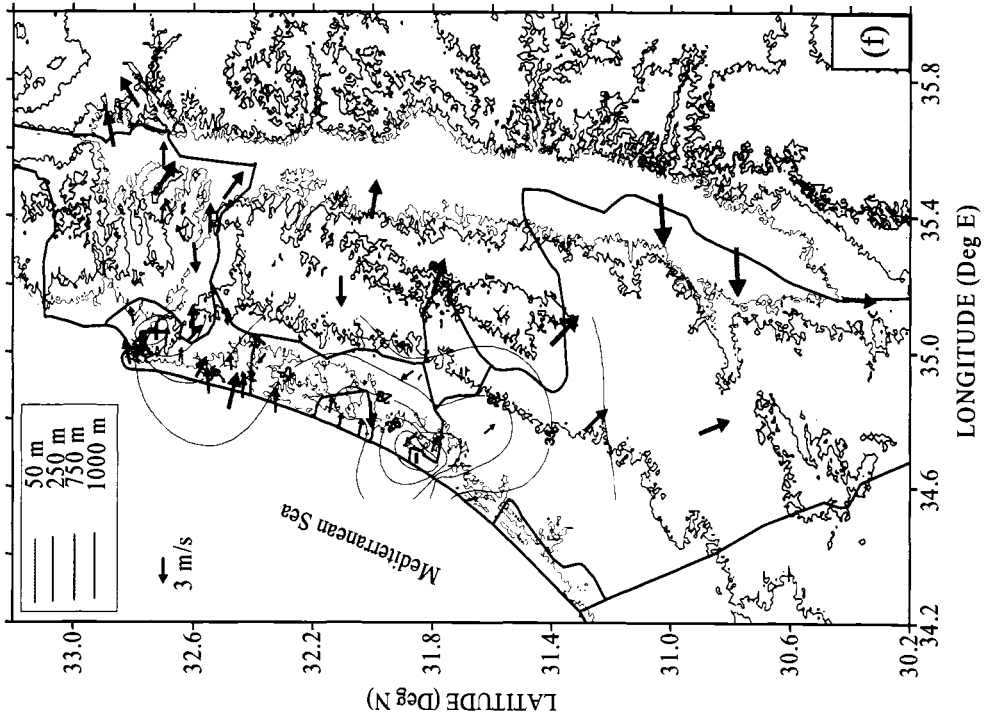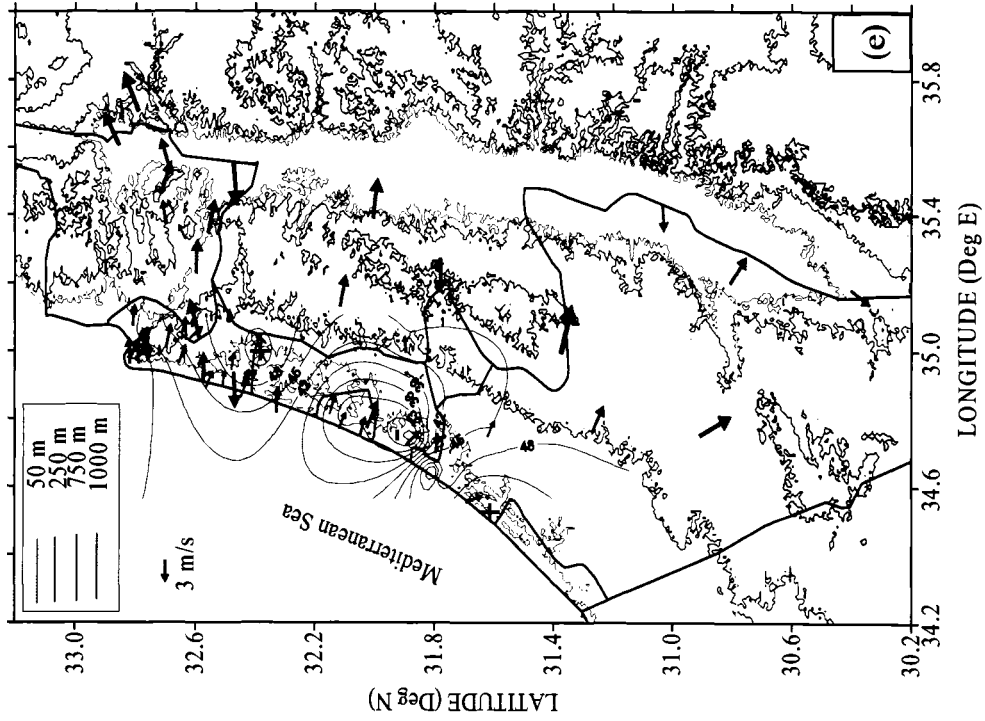
Fig. 26. Observed surface O_3 (ppb) and winds on 1 August 1997 at:
(e) 2000 and (f) 2300 LST

76
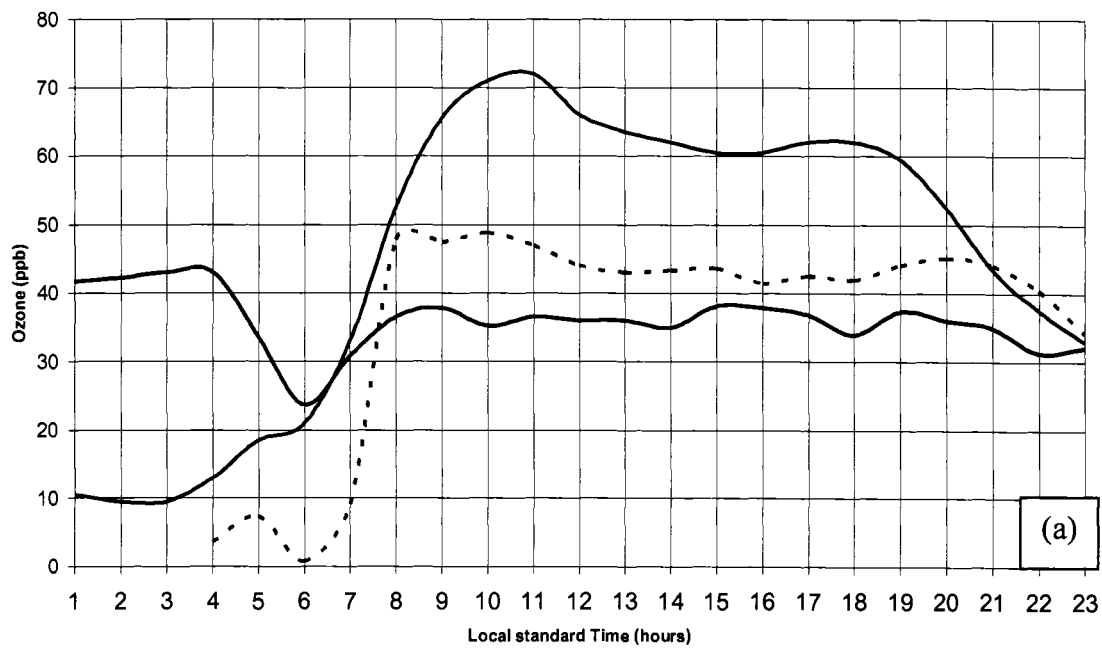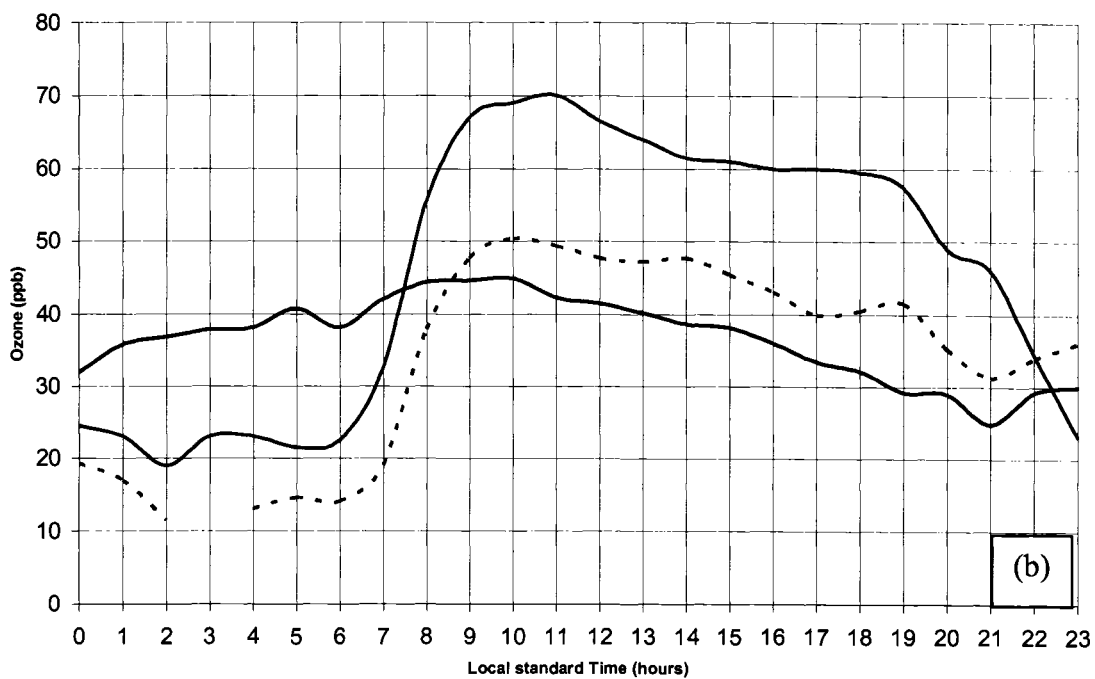
Fig. 27. Surface observed O_3 time series for August 1997 on:

(a) 1 August and (b) 2 August

77
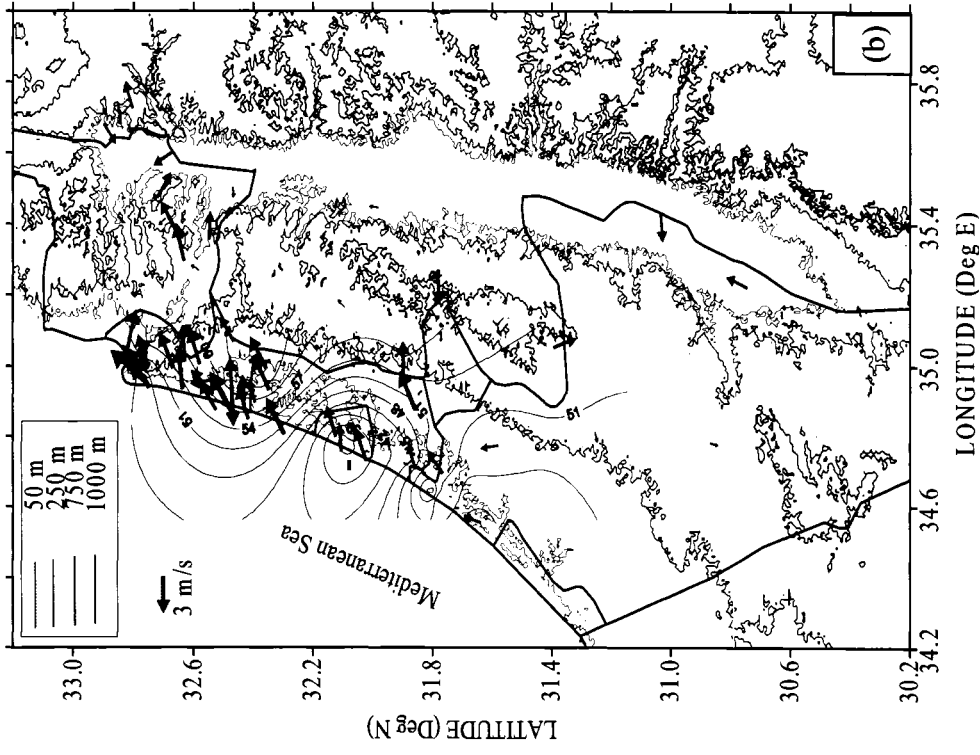
Fig. 28. Observed surface O₃ (ppb) and winds on 2 August 1997 at:

(a) 0300 and (b) 0900 LST

78

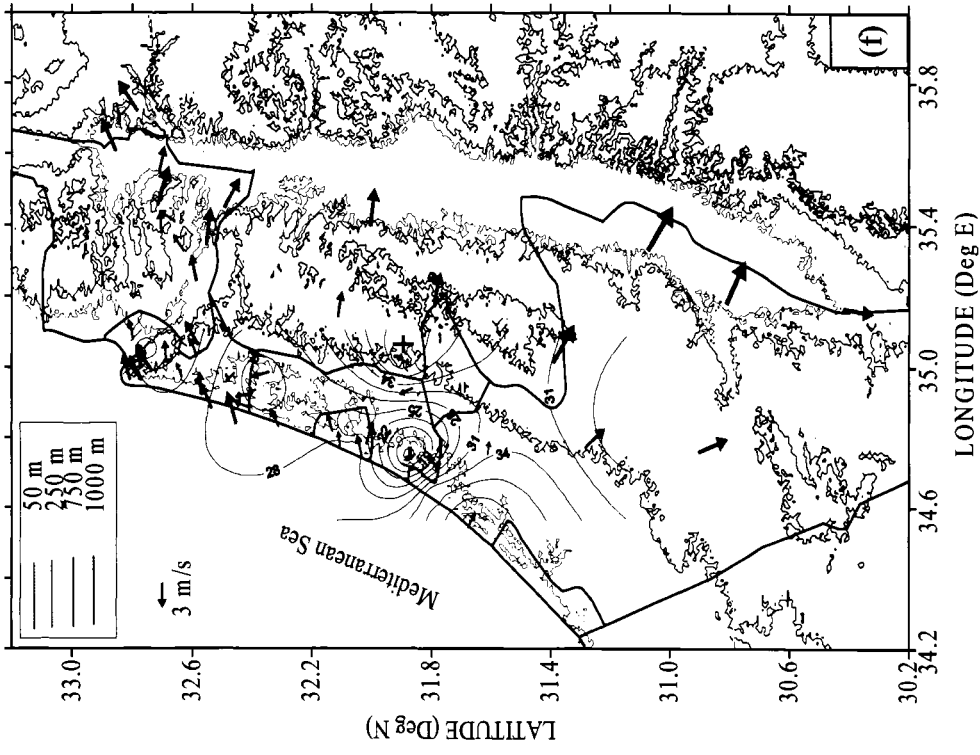Fig. 28. Observed surface O$_3$ (ppb) and winds on 2 August 1997 at:
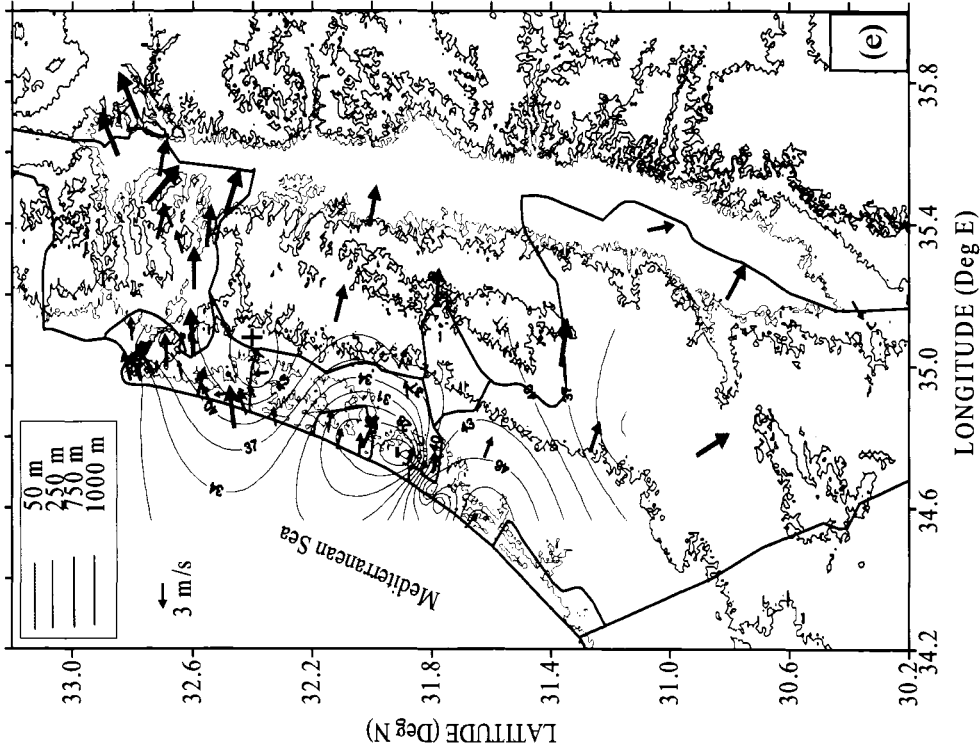
(c) 1100 and (d) 1600 LST

Fig. 28. Observed surface O_3 (ppb) and winds on 2 August 1997 at:

(e) 2000 and (f) 2300 LST